NASA Contractor Report 3884

Numerical Study of Large-Eddy Breakup and Its Effect on the Drag Characteristics of Boundary Layers

Robert B. Kinney, Mohammad E. Taslim,
and Shi Chang Hung

GRANT NAG1-141
MARCH 1985

NASA

NASA Contractor Report 3884

Numerical Study of Large-Eddy Breakup and Its Effect on the Drag Characteristics of Boundary Layers

Robert B. Kinney, Mohammad E. Taslim,
and Shi Chang Hung
University of Arizona
Tucson, Arizona

Prepared for
Langley Research Center
under Grant NAG1-141

National Aeronautics
and Space Administration

**Scientific and Technical
Information Branch**

1985

TABLE OF CONTENTS

LIST OF FIGURES

NOMENCLATURE

$a,b, \ldots, i$	Coefficients use in biquadratic interpolation of stream function
$f(\eta)$	Dimensionless stream function in Blasius solution of flat-plate boundary-layer equations
$f(\theta)$	Function appearing in complementary solution for bound vorticity
h_1, h_2	Horizontal spacing between nodes, Fig. B-1
k_1, k_2	Vertical spacing between nodes, Fig. B-1
$\vec{k}$	Unit vector perpendicular to plane of flow
K_I, K_{II}	Kernel functions appearing in velocity induction law, Eqns. (20) and (21)
ℓ_c	Virtual distance of eddy center upstream of computational domain.
L	Length of eddy break-up plate, Fig. 1
$\vec{r}$	Vector radius pointing from vortex element to a point in the flow
Re	Reynolds number, $U_\infty L/\nu$
S	Elevation of eddy break-up plate above the wall, Fig. 1
t	Dimesionless time, $t^* U_\infty / L$

NOMENCLATURE (continued)

t'	Dummy variable of integration in Eqn. (18)
u	Dimensionless fluid velocity in x-direction, u^*/U_∞
U_∞	Undisturbed free-stream velocity in x-direction
U_b	Velocity of undisturbed background flow given by Blasius solution
U_{slip}	Apparent slip velocity induced at solid surfaces by the free vorticity, ω
v	Dimensionless fluid velocity in y-direction, v^*/U_∞
$\vec{V}$	Dimensionless velocity vector (u,v)
x	Dimensionless coordinate measured along the wall from plate centerline, x^*/L, Fig. 1
x'	Streamwise coordinate measured from virtual origin of wall boundary layer
y	Dimensionless coordinate measured perpendicular to the wall along the plate centerline, y^*/L
γ	Dimensionless bound vorticity of the eddy break-up plate, $\vec{\gamma} = \gamma \vec{k}, \hat{\gamma}$ is auxiliary bound vorticity given by $\gamma \sin\theta$, $\gamma = \gamma^*/U_\infty$
δ	Boundary layer thickness, equal to 2L
η	Stretched y-coordinate in Blasius boundary-layer solution

NOMENCLATURE (continued)

θ	Polar angle on circumscribed circle about the plate, measured from downstream edge
ν	Kinematic viscosity of the fluid
ϕ	Velocity potential of the irrotational flow
ψ	Dimensionless stream function, $\psi^*/U_\infty L$
ψ'	Dimensionless stream function of the perturbation flow, Eqn. (19)
ω	Dimensionless vorticity, $\omega^* L/U_\infty$
ω'	Dimensionless perturbation vorticity, $\omega - \Omega_b$
Ω_b	Dimensionless vorticity of the background flow as obtained from Blasius solution

Superscript

*	Denotes dimensional quantity

Subscripts

wall, w	Denotes evaluated at the wall
plate	Denotes evaluated at the plate
part	Denotes particular solution
comp	Denotes complementary solution

ABSTRACT

The break-up of a field of eddies by a flat-plate obstacle embedded in a boundary layer is studied using numerical solutions to the two-dimensional Navier-Stokes equations. The flow is taken to be incompressible and unsteady.

The flow field is initiated from rest. A train of eddies of predetermined size and strength are swept into the computational domain upstream of the plate. The undisturbed velocity profile is given by the Blasius solution. The disturbance vorticity generated at the plate and wall, plus that introduced with the eddies, mix with the background vorticity and is transported throughout the entire flow.

All quantities are scaled by the plate length, the undisturbed free-stream velocity, and the fluid kinematic viscosity. The Reynolds number is 1000, the Blasius boundary layer thickness is 2.0, and the plate is positioned a distance of 1.0 above the wall. The computational domain is four units high and sixteen units long.

A hybrid solution method is used for the velocity field. The velocity induction law is used to determine boundary velocities along the solid surfaces and on the perimeter of the computational domain. Nonzero tangential velocities at solid surfaces are cancelled by the proper amount of vorticity production. The velocity field inside the domain is computed from the streamfunction.

Results are presented over the range of time 0 to 14.61. Vorticity contour plots are used to visualize the eddy break-up. Marker particles are also used to help visualize the overall flow. A plot of total drag variation with time is also given.

Results show that the eddies are broken up by the plate. The strong wake generated by the plate prevents the eddy vorticity from penetrating the region between the plate and wall as the eddies are swept downstream. Transverse velocities evident ahead of the plate are absent behind the plate. Thus, it appears that high speed outer fluid is prevented by the plate from being entrained into the fluid layer near the wall. This has been proposed to be one of the mechanisms by which break-up devices can reduce drag locally. The numerical predictions support this proposal.

I. INTRODUCTION

Interest in reducing the drag of aerodynamic surfaces has led to a new examination of the fundamental transport processes occuring in turbulent boundary layers. It has been hypothesized that the proper management of the large scale turbulence can affect wall variables such as skin friction. Of particular interest are the large eddy-like structures which are believed to entrain the high speed outer potential flow into the boundary, thereby causing momentarily high velocities to occur near the wall. These higher velocities in turn lead to locally high values of the skin friction.

Whereas there is not as yet universal acceptance of the concept that large-scale structures are associated with high skin friction, recent important experiments by Nagib and co-workers at the Illinois Institute of Technology lend strong support to this concept. Corke, Nagib, and Guezennec [1] have found that the outer scales, defined by the intermittent excursions of potential fluid into the boundary layer, can be suppressed by simple arrangements of parallel plates. This results in a decrease in the streamwise growth of the boundary-layer thickness (also the momentum thickness), leading to a decrease in the local wall shear stress. They report a 30% decrease in local skin-friction coefficient. When account is made of the viscous drag of the plates, the overall drag reduction is 20%.

The authors of Ref. 1 speculate that the large outer scales are remnants of the laminar-turbulent transition process. These are slowly decaying structures that are embedded in the boundary layer. The plates

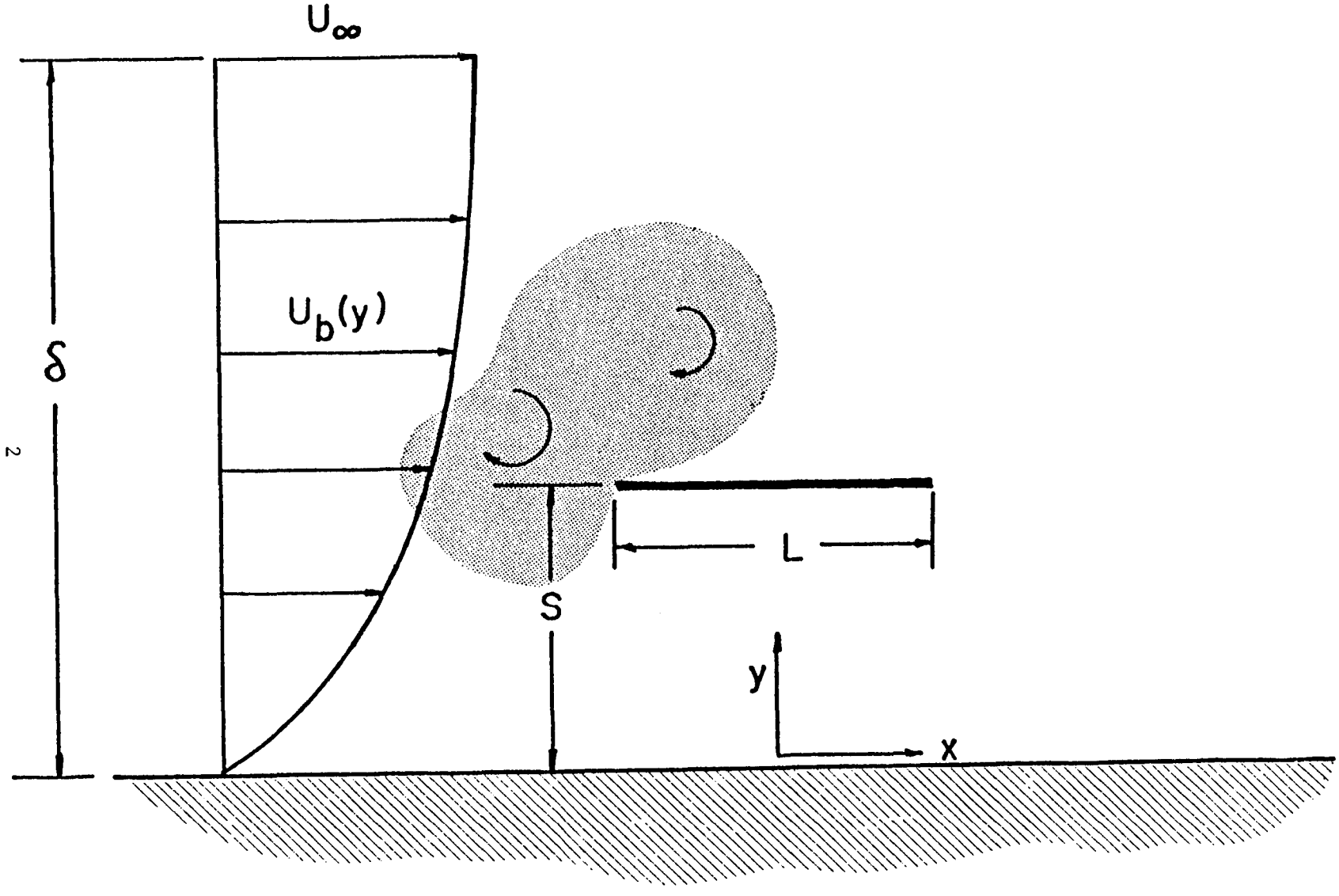

Fig. 1 Schematic Diagram of Flow Configuration

mechnically suppress potential fluid entrainment and thus hasten the Reynolds number aging of the boundary layer. The result is a reduced growth rate of the boundary-layer thickness with downstream distance.

The essentially two-dimensional dynamical interpretation given by Corke et al. may be an oversimplification of a much more complicated three-dimensional flow. However, the basic concept appears to be sound. Four mechanisms, by which the plates act to suppress the outer scales, have been given by the authors. These can be summarized as follows: 1) restriction of the vertical velocity components in the boundary layer, 2) generation by the plate of unsteady circulation opposite to that of the large-scale motions, 3) generation of a small-scale vortex street behind the plate, and a redistribution of small-scale turbulence, and 4) small-scale turbulence production due to the wake of the plates embedded in a much thicker wall boundary layer. These above-mentioned mechanisms are not all independent, and when account is taken of the unsteady nature of the flow and the many scales of turbulence present, it is difficult to identify which ones are dominant.

The present study was undertaken in order to identify the basic dynamical processes which occur when eddy-like structures interact with a flat plate embedded in a boundary layer. The approach is numerical rather than experimental and is based on solutions to the unsteady two-dimensional Navier-Stokes equations for incompressible flow. The intent is not to simulate a fully turbulent flow by numerical means, nor is any turbulence modeling incorporated into the analysis. Rather, an analysis is made of a

flow which has several gross features in common with the boundary-layer flow studied experimentally in [1].

The eddy-like structures are taken to be regions of constant vorticity which are initially circular in shape. They distort in the shear flow as they are convected towards a single flat-plate manipulator positioned parallel to a wall of large extent. A sequence or train of eddies is introduced computationally ahead of the plate. The eddies have varying strengths and length scales, the latter being on the order of the boundary-layer thickness, δ. These length scales are comparable to those found in the experiments of [1].

The eddies are superimposed onto an otherwise steady background flow which is laminar. In this way, a flow is produced which is close to that in a laminar boundary layer undergoing transition. Thus, it is not as developed as that produced experimentally in [1]. Also, the Reynolds number based on the boundary-layer thickness is 2000, which is approximately 1600 when based on the momentum boundary-layer thickness. This latter quantity ranged from about 2200 to 5000 in the experiments of [1]. Therefore, this parameter for the present study is close to the low end of the range studied in the experiments.

II. BASIS OF THEORETICAL APPROACH

The basic approach is the same as that incorporated by Schmall and Kinney [2]. However, rather than the flat plate being positioned in a uniform onset flow, in this work it is imbedded in an unsteady viscous flow adjacent to a plane surface. This necessitates the introduction of image vorticity in order to satisfy boundary conditions. As in [2], the plate is replaced by a distribution of bound vorticity, and the vorticity production at solid surfaces (plate plus lower bounding wall) is calculated directly.

The velocity field is calculated using a hybrid scheme which incorporates the stream function and velocity induction law. The velocity induction law is used to obtain the effect of the bound vorticity of the plate on the main flow, as well as the tangential velocity induced at solid surfaces. This latter quantity is needed in the determination of the vorticity production. The rotational velocity of the main flow is computed from the stream function, as obtained from the numerical solution of Poisson's equation.

The analytical development is given in the next section. The working equations are presented, and the numerical formulation is discussed. Lengthy developments are given in the various appendices.

III. ANALYSIS

A schematic of the flow configuration is shown in Fig. 1. The characteristic length scale for the flow is taken to be the plate length, L. We have selected $S = L$ and $\delta = 2L$. The background velocity profile is denoted by $U_b(y)$. This is taken to be the Blasius profile for laminar flow on a flat plate with zero pressure gradient.

Strictly speaking, δ and U_b are functions of x. However, over the region of interest, their streamwise variation is very small. This can be seen if the characteristic Reynolds number is introduced as $Re = U_\infty L / \nu$ where a value of 1000 has been chosen for this study.

Let x' be the streamwise distance measured from the virtual origin of the boundary layer on the wall. One has for a Blasius profile that $\delta/x' \cong 6/(U_\infty x'/\nu)^{1/2}$. Then $\delta/L = 6[(x'/L)/(U_\infty L/\nu)]^{1/2}$. Upon substitution of $\delta/L = 2$ and $U_\infty L/\nu = 1000$, one obtains $x'/L = 111$. Therefore, the virtual origin of the boundary layer is more than 100 plate-lengths upstream of the plate. As will be discussed more fully later, the domain of interest spans a region which is 16 plate-lengths in the flow direction. Over this distance, the boundary layer grows only 7%. This is a low order effect, and therefore the variation of δ and U_b in the streamwise direction has been neglected entirely.

The other quantities of interest are the vorticity of the background flow and the relative distance y/L, where y is measured from the wall. One begins with the boundary-layer approximation $\Omega_b = -\partial U_b / \partial y$, where now U_b is considered to be a function of η,

and $\eta = (y/x')(U_\infty x'/\nu)^{1/2}$. Recall that $U_b = U_\infty f'(\eta)$, where $f'(\eta)$ is the derivative of the dimensionless stream function. Clearly, $\Omega_b \approx -U_\infty f''(\eta)\, \partial\eta/\partial y$, from which $\Omega_b L/U_\infty = -f''(\eta)\, [(x'/L)/(U_\infty L/\nu)]^{-1/2}$ is the dimensionless background vorticity. From the foregoing expression for δ/L, one has $[(x'/L)/(U_\infty L/\nu)]^{1/2} = 1/3$. Therefore, $\Omega_b L/U_\infty = -3\, f''(\eta)$. One can also show that $\eta = (y/L)\, [x'/L)\, (U_\infty\, L/\nu)]^{-1/2}$, from which $y/L = \eta/3$. When $\eta = 6$, then $y = \delta$ and $\delta/L = 2$ as required.

To summarize, then, we have

$$U_b = U_\infty f'(\eta) \tag{1}$$

$$\Omega_b L/U_\infty = -3\, f''(\eta) \tag{2}$$

$$y/L = \eta/3 \tag{3}$$

The values of η, $f'(\eta)$, and $f''(\eta)$ are given in tabular form in Ref [3], Page 139. In practice, it is the value of y/L which is specified in the calculations. From this, η is obtained from (3), and the values of $f'(\eta)$ and $f''(\eta)$ are obtained by interpolation.

Governing Equations

Superimposed onto the background flow are perturbation velocity and vorticity fields caused by the presence of the plate, as well as the coherent eddy structures introduced ahead of the plate. We denote as u' and v' the x- and y-components of perturbation velocity, and ω' denotes the perturbation vorticity field. Then

$$u = U_b(y) + u'(x,y,t) \tag{4}$$

$$v = v'(x,y,t) \tag{5}$$

$$\omega = \Omega_b(y) + \omega'(x,y,t) \tag{6}$$

No assumption is made that these perturbation quantities are small.

The vorticity transport equation is given by

$$\frac{\partial \omega}{\partial t} + \frac{\partial}{\partial x}(u\omega) + \frac{\partial}{\partial y}(v\omega) = \frac{1}{Re}\left(\frac{\partial^2 \omega}{\partial y^2} + \frac{\partial^2 \omega}{\partial x^2}\right) \tag{7}$$

and the continuity equation is

$$\frac{\partial u}{\partial x} + \frac{\partial v}{\partial y} = 0 \tag{8}$$

At this point, all independent and dependent variables have been rendered nondimensional using U_∞, L, and ν. That is, $t = t^*U_\infty/L$, $u = u^*/U_\infty$, $y = y^*/L$, $\omega = \omega^*L/U_\infty$, etc. The asterisk denotes a dimensional variable, which will normally be omitted for convenience. The origin of the x and y coordinates is as shown in Fig. 1.

Note that Eqn. (7) allows the background vorticity, Ω_b, to be transported by convection and diffusion in the lateral direction only, since it does not depend on x. Therefore, there is a mechanism by which Ω_b can change with time. Nevertheless, the effect is small and is of no real importance. Therefore, it has been neglected here.

The velocity field is obtained from a hybrid formulation in terms of the stream function and/or the velocity induction law, referred to here

as the Biot-Savart law. The general form for the x-component can be written as

$$u(x_p,y_p t) = \frac{1}{2\pi} \iint \frac{\omega\,(y-y_p)}{(x-x_p)^2 + (y-y_p)^2}\, dx\, dy + \vec{i}\cdot\text{grad}\,\phi \qquad (9)$$

where P is some point in the flow, and the range of integration is over the region of non-zero vorticity. Note that this expression contains $\vec{i}\cdot\text{grad}\,\phi$, which must be included for generality. More will be said about this term later. The expression for the y-component of velocity is

$$v(x_p,y_p,t) = -\frac{1}{2\pi} \iint \frac{\omega\,(x-x_p)}{(x-x_p)^2 + (y-y_p)^2}\, dx\, dy + \vec{j}\cdot\text{grad}\,\phi \qquad (10)$$

It is easily verified that $\text{curl}_p \vec{V} = \vec{k}\,\omega$, where the curl operator is with respect to the coordinate at P.

The term grad ϕ is a purely irrotational contribution to the velocity field and must be included to insure that boundary conditions are satisfied. The principal velocity boundary conditions embody the adherence condition at solid surfaces. These are enforced in two steps. First, the normal velocity component is nullified, after which the tangential component is reduced to zero. The first step is accomplished through image vorticity plus the proper specification of grad ϕ. The second step is accomplished through the proper production of vorticity at the solid surfaces.

We require that v vanish on the solid wall and plate. The wall is taken to be a plane of anti-symmetry such that below it we have vorticity which is opposite in sign to that above the wall. This concept of image

vorticity provides a straightforward means for determining grad ϕ in (9) and (10).

Any irrotational velocity field which produces zero normal velocity at the plate and wall will satisfy the requirements for grad ϕ. Therefore, we replace the plate by a distribution of bound vorticity, $\vec{\gamma}$, along its length. A distribution of fluid sources would do as well, but the vorticity distribution better satisfies our needs. Therefore, we make the following substitution.

$$\text{grad } \phi = \frac{1}{2\pi} \int_{-1/2}^{1/2} \frac{\vec{\gamma} \times \vec{r}}{r^2} \, dx \tag{11}$$

where $\vec{r}$ is the vector from γ to the point P, and dx is the incremental plate length over which γ is distributed. Also, $\vec{\gamma} = \vec{k}\,\gamma$.

To produce the proper anti-symmetry about the wall, we replace ω and γ in the lower half plane ($y' < 0$) by their images. Therefore, we have

$$u(x_p,y_p,t) = \frac{1}{2\pi} \int_0^{+\infty} \int_{-\infty}^{+\infty} \omega \left[\frac{y-y_p}{(x-x_p)^2 + (y-y_p)^2} + \frac{y+y_p}{(x-x_p)^2 + (y+y_p)^2} \right] dx\, dy$$

$$+ \frac{1}{2\pi} \int_{-1/2}^{+1/2} \gamma \left[\frac{s-y_p}{(x-x_p)^2 + (s-y_p)^2} + \frac{s+y_p}{(x-x_p)^2 + (s+y_p)^2} \right] dx \tag{12}$$

$$v(x_p,y_p,t) = -\frac{1}{2\pi} \int_0^{+\infty} \int_{-\infty}^{+\infty} \omega \left[\frac{x-x_p}{(x-x_p)^2 + (y-y_p)^2} - \frac{x-x_p}{(x-x_p)^2 + (y+y_p)^2} \right] dx\, dy$$

$$- \frac{1}{2\pi} \int_{-1/2}^{+1/2} \gamma \left[\frac{x-x_p}{(x-x_p)^2 + (s-y_p)^2} - \frac{x-x_p}{(x-x_p)^2 + (s+y_p)^2} \right] dx \tag{13}$$

To obtain (12) and (13), one replaces ω with $-\omega$ and γ with $-\gamma$ in the lower half plane. The range of integration on y is then changed to include only the positive half-plane $y \geq 0$.

It is clear from (13) that $v = 0$ whenever $y_p = 0$. That is, the wall is a streamline. Note, however, that $u \neq 0$ when $y_p = 0$, and there is an apparent slip velocity on the wall (there is also one on the plate). This must be reduced to zero by the proper production of free vorticity at the wall and plate. This process will be discussed subsequently.

The distribution for γ must be so constituted that no transverse velocity exists at the plate. To obtain the governing equation for γ, one sets $y_p = S$ in (13), and sets the left-hand side to zero. There results an integral equation for γ as follows:

(14)

$$\int_{-1/2}^{+1/2} \gamma\left[\frac{1}{x-x_p} - \frac{x-x_p}{(x-x_p)^2 + 4s^2}\right]dx = -\int_0^{+\infty}\int_{-\infty}^{+\infty} \omega'\left[\frac{x-x_p}{(x-x_p)^2 + (y-y_p)^2} - \frac{x-x_p}{(x-x_p)^2 + (y+y_p)^2}\right]$$

When it is solved, the resulting velocity field satisfies all the requirements of the problem, except possibly the no-slip condition on the wall and plate. As mentioned earlier, this must be reduced to zero in the calculation of the free vorticity from (7).

For the evaluation of the apparent slip velocities at solid surfaces, one uses (12). It is expedient to introduce $\omega = \Omega_b(y) + \omega'(x,y,t)$ into (12) and to note that the integration of $\Omega_b(y)$ over the infinite domain produces only the background velocity, $U_b(y_p)$. Therefore, we add $U_b(y_p)$ to the right-hand side of (12) and replace ω by ω'. Next,

we set $y_p = 0$ and evaluate $u(x_p,0,t)$. Let us call this $(U_{slip})_{wall}$. Thus,

$$(U_{slip})_{wall} = \frac{1}{2\pi} \int_0^{\infty} \int_{-\infty}^{\infty} \omega' \frac{2y}{(x-x_p)^2 + (y-y_p)^2} \, dx \, dy$$

$$+ \frac{1}{2\pi} \int_{-1/2}^{1/2} \gamma \left[\frac{2S}{(x-x_p) + (S-y_p)^2} \right] dx \tag{15}$$

The evaluation of the slip velocity on the plate is slightly more involved. First, set $y_p = S^+$ in (12), where S^+ is a small distance ε above the plate. The integration of ω is straightforward. The integration of the first term involving γ must be done carefully, since $y = S$, and thus $S - y_p = -\varepsilon$. As $\varepsilon \to 0$ we obtain $-\gamma/2$ for this integral. When $y_p = S^-$, we obtain $+\gamma/2$ for this integral. Thus there is a different apparent slip velocity on the upper and lower surfaces of the plate. The end result is

$$(U_{slip})^+_{plate} = U_b(s) + \frac{1}{2\pi} \int_0^{+\infty} \int_{-\infty}^{+\infty} \omega' K_I(x,y,x_p,y_p) \, dx \, dy$$

$$- \frac{1}{2} \gamma (x_p) + \frac{1}{2\pi} \int_{-1/2}^{+1/2} \gamma(x) \left[\frac{2S}{(x-x_p)^2 + 4S^2} \right] dx \tag{16}$$

$$(U_{slip})^-_{plate} = (U_{slip})^+_{plate} + \gamma(x_p) \tag{17}$$

where K_I is the quantity in brackets in (12).

Once the slip velocities are determined for the wall and plate surfaces, the vorticity production is given by

$$\int_{t}^{t+\Delta t} \frac{1}{Re}\left(\frac{\partial \omega'}{\partial y}\right)_{surface} dt' = (U_{slip})_{surface} \qquad (18)$$

This follows the scheme used by Schmall and Kinney [2]. The convention is to evaluate the right-hand side of (18) at time t. Also, a positive slip velocity on the upper portion of a surface produces negative free vorticity, whereas the reverse is true on the lower portion of a surface.

Equation (18) is the essential surface boundary condition needed in the solution of (7). The manner in which it is implemented is discussed in the next section.

As mentioned earlier, a hybrid formulation was finally used for the calculation of the velocity field at interior points of the flow. This involved the use of the stream function for a part of the evaluations, as is now explained.

The integral involving ω, or equivalently ω', in (12) can be cast in terms of the stream function. All that is required is that this integral give a rotational velocity field which has the correct amount of vorticity at each fluid point and which satisfies the boundary conditions. That is, we can replace this integral with $U_b(y_p) + \partial\psi'/\partial y$, where ψ' is the perturbation stream function which satisfies the Poisson equation

$$\frac{\partial^2 \psi'}{\partial x^2} + \frac{\partial^2 \psi'}{\partial y^2} = -\omega' \qquad (19)$$

It turns out that the evaluation of $\partial\psi'/\partial y$ is computationally more efficient than the evaluation of the integral involving ω' in (12), when the domain of integration is large. It remains to ensure that the proper boundary conditions are specified for ψ' or its derivatives.

We first write

$$\frac{\partial\psi'}{\partial y} = \frac{1}{2\pi} \int_{0}^{+\infty} \int_{-\infty}^{+\infty} \omega' \, K_I(x,y,x_p,y_p) \, dx \, dy \tag{20}$$

$$\frac{\partial\psi'}{\partial x} = \frac{1}{2\pi} \int_{0}^{+\infty} \int_{-\infty}^{+\infty} \omega' \, K_{II}(x,y,x_p,y_p) \, dx \, dy \tag{21}$$

where K_I and K_{II} are the quantitites in brackets in (12) and (13), respectively.

For a given ω', (20) or (21) give the value of the normal derivatives of ψ' at points on the boundary of the domain, inside of which ψ' is defined by (19). That is, if y_p is set to the value 4.0, then (20) gives the value of $\partial\psi'/\partial y$, at points x_p along the top (horizontal) boundary of the domain. Similarly, for fixed x_p, (21) gives the value of $\partial\psi'/\partial x$ at points y_p along the side (vertical) boundaries of the domain. On the wall, we set $\psi' = 0$, since this must be a streamline.

The boundary condition along the wall is of the Dirichlet type, whereas those along the sides and top are of the Neumann type. It is known that the solution to (19), subject to these boundary conditions, is unique.

Before turning to the numerical formulation, a few comments concerning the evaluation of γ are in order. Recall that the integral equation for γ is given by (14). The vorticity field, ω', is known. The

solution for γ induces a purely potential (i.e., irrotational) velocity field, which corresponds to that produced by a flat plate in ground effect. In this case, the velocity induced at the plate by ω' is simply a given input quantity equivalent to an outer onset-flow velocity.

As $S \to \infty$, the solution for γ must approach that for a single plate in unconfined flow. It is equivalent to that given in classical aerodynamics and used by Schmall and Kinney [2]. Therefore, the general form is already known from classical theory.

The essential point to keep in mind here is that the solution for γ is non-unique and must contain a term corresponding to pure circulatory flow about the plate. For a single plate, this term is $A/\sin\theta$. Here A is a constant and θ is a polar angle obtained by circumscribing a circle about the plate so that the plate is coincident with a diameter. The angle θ is measured from the plate in the counterclockwise direction. For a plate in ground effect (i.e., there are two plates when the image is introduced), the solution corresponding to the pure circulatory flow is of the form $A\, f(\theta)/\sin\theta$. Clearly, $f(\theta) \to 1$ as $S \to \infty$. Unfortunately, $f(\theta)$ is not given in terms of elementary functions. However, it is easily determined numerically. It is found by solving the integral equation for γ when the non-homogeneous term is omitted. The non-homogeneous term corresponds to the velocity induced by ω'. The resulting solution for γ to the homogeneous equation is called the complementary solution.

The unknown constant A is determined from the principle of conservation of total vorticity (see Ref. [2]. Simply stated,

$$\int_{-1/2}^{+1/2} \gamma \, dx = \int_{0}^{\pi} \hat{\gamma}(\theta) d\theta = 0 \qquad (22)$$

where $\gamma = \hat{\gamma}/\sin\theta$. Recalling that γ (or $\hat{\gamma}$) is composed of a particular solution to the complete (i.e. non-homogeneous) integral equation plus the complementary solution [i.e. $\hat{\gamma} = \hat{\gamma}_{part} + A\, f(\theta)$], A can be determined to be

$$- \frac{\int_{0}^{\pi} \hat{\gamma}_{part}(\theta)\, d\theta}{\int_{0}^{\pi} f(\theta)\, d\theta} \qquad (23)$$

where it is convenient to carry out the integrations in the θ-plane.

Numerical Formulation

A complete description of the computational domain is given in the section dealing with the numerical parameters. Briefly, it is rectangular in shape. It extends from $x = -4$ to $x = +12$, and $y = 0$ to $y = 4$. A view of the region near the plate ($-4 \leq x \leq 4$) is given in Fig. 2. The plate is positioned at $y = 1$, and it covers the range $-1/2 \leq x \leq +1/2$. The background velocity field is confined to the region $0 \leq y \leq 2$. That is, δ in Fig. 1 is equal to 2.0.

It is assumed that ω' is zero above the computational domain $y > 4$. Furthermore, ω' is set equal to zero ahead of the upstream boundary ($x < -4$) and behind the downstream boundary ($x > 12$). At $x = 12$ we have imposed the condition $\partial\omega'/\partial x = 0$.

The grid is refined near the wall and plate in the transverse direction, and near the leading and trailing edges of the plate in the streamwise direction. Furthermore, the plate is discretized along its

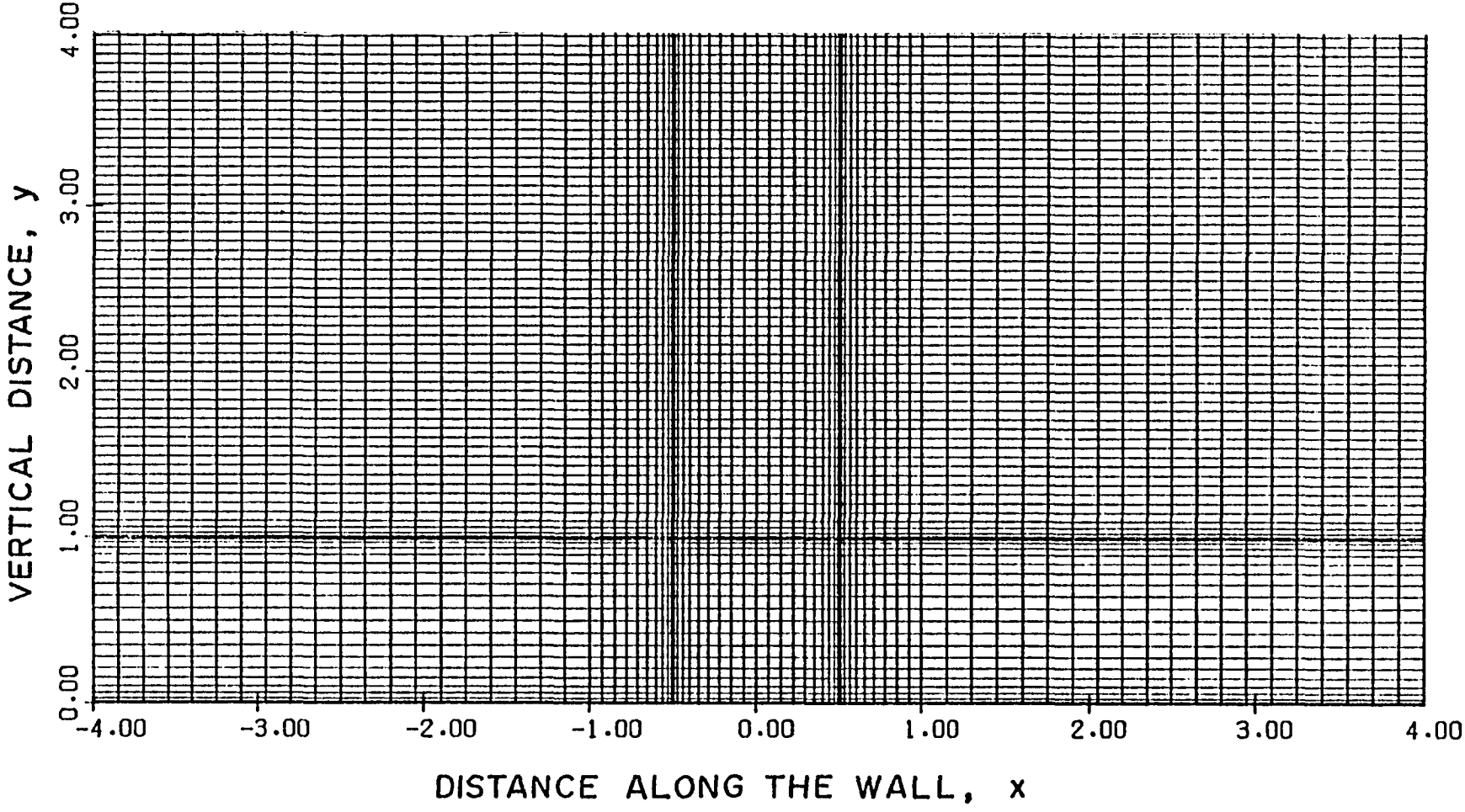

Fig. 2 Computational Domain Near the Plate

length independently of the outer-flow grid. There are 20 fluid cells in contact with the plate, whereas there are 80 points along the plate at which γ is determined.

Solution for Bound Vorticity. The solution for γ is obtained at 80 discrete points on the surface of the plate. The polar angle θ is introduced, and the 80 points are obtained by first constructing arcs of length $\Delta\theta$ on the circle of unit diameter, where $\Delta\theta = \pi/80$. Points are positioned at the centers of each arc around the circle, and these are projected vertically downward onto the diameter, which comprises the plate. In this way, there is a clustering of vortex points on the plate near the leading and trailing edges.

A polar coordinate system is used in which $x = .5\cos\theta$ and $dx = -.5\sin\theta d\theta$. The integral equation for γ, Eqn. (14), is evaluated at each of 80 points given by $x_p = .5\cos\theta_p$. The solution is actually determined for $\hat{\gamma}$ $(=\gamma\sin\theta)$ rather than γ, and $\hat{\gamma}$ is assumed to be constant over an interval $\Delta\theta$. When this is substituted into each of the 80 integral equations, there results a system of 80 simultaneous equations in 80 unknowns, $\hat{\gamma}_i$.

As previously mentioned, the general solution is composed of particular and complementary solutions. Since each is non-unique, we can assign an arbitrary value to one of the 80 unknowns in each solution.

For convenience, we set the 80th unknown in each set to 1.0 and solve the two sets of equations. If $f(\theta)$ denotes the solution to the homogeneous equations, then $\hat{\gamma}_{comp} = A\, f(\theta)$. The constant A is determined from Eqn. (23).

Solution for Free Vorticity. The solution of Eqn. (7) is straightforward. We first integrate (7) with respect to space over a fluid element $\Delta x \Delta y$. This gives

$$\frac{\partial}{\partial t}\iint \omega \, dx \, dy = -\iint \text{div}\,[\vec{i}\, u\, \omega + \vec{j}\, v\, \omega]\, dx\, dy + \frac{1}{Re}\iint \text{div}\,(\text{grad}\,\omega)\, dx\, dy \tag{24}$$

By the divergence theorem,

$$\iint \text{div}\,[\vec{i}\, u\, \omega + \vec{j}\, v\, \omega]\, dx\, dy = \int_{y}^{y+\Delta y} [(-u\omega)_x + (u\omega)_{x+\Delta x}]\, dy + \int_{x}^{x+\Delta x} [(-v\omega)_y + (v\omega)_{y+\Delta y}]\, dx \tag{25}$$

and

$$\iint \text{div}\,(\text{grad}\,\omega)\, dx\, dy = \int_{y}^{y+\Delta y} \left[\left(-\frac{\partial \omega}{\partial x}\right)_x + \left(\frac{\partial \omega}{\partial x}\right)_{x+\Delta x}\right] dy + \int_{x}^{x+\Delta x} \left[\left(-\frac{\partial \omega}{\partial y}\right)_y + \left(\frac{\partial \omega}{\partial y}\right)_{y+\Delta y}\right] dx \tag{26}$$

We apply the mean-value theorem, which leads to the approximation

$$\int_{y}^{y+\Delta y} \left(\frac{\partial \omega}{\partial x}\right)_{x+\Delta x} dy \cong \left(\frac{\partial \omega}{\partial x}\right)_{\substack{x+\Delta x \\ y+\Delta y/2}} \Delta y \tag{27}$$

and so forth for each of the terms in (25) and (26). If subscripts i and j denote the variables evaluated at points in the vicinity of a fluid cell, as shown in Fig. 3, then we can write further that

$$\int_{y}^{y+\Delta y} \left(\frac{\partial \omega}{\partial x}\right)_{x+\Delta x} dy \cong \left[\frac{\omega_{i+1,j} - \omega_{i,j}}{.5(\Delta x_i + \Delta x_{i+1})}\right] \Delta y_j \tag{28}$$

$$\frac{\partial}{\partial t}\int \omega \, dx \, dy \cong \frac{\partial}{\partial t}\,[\omega_{i,j}]\, \Delta x_i\, \Delta y_j \tag{29}$$

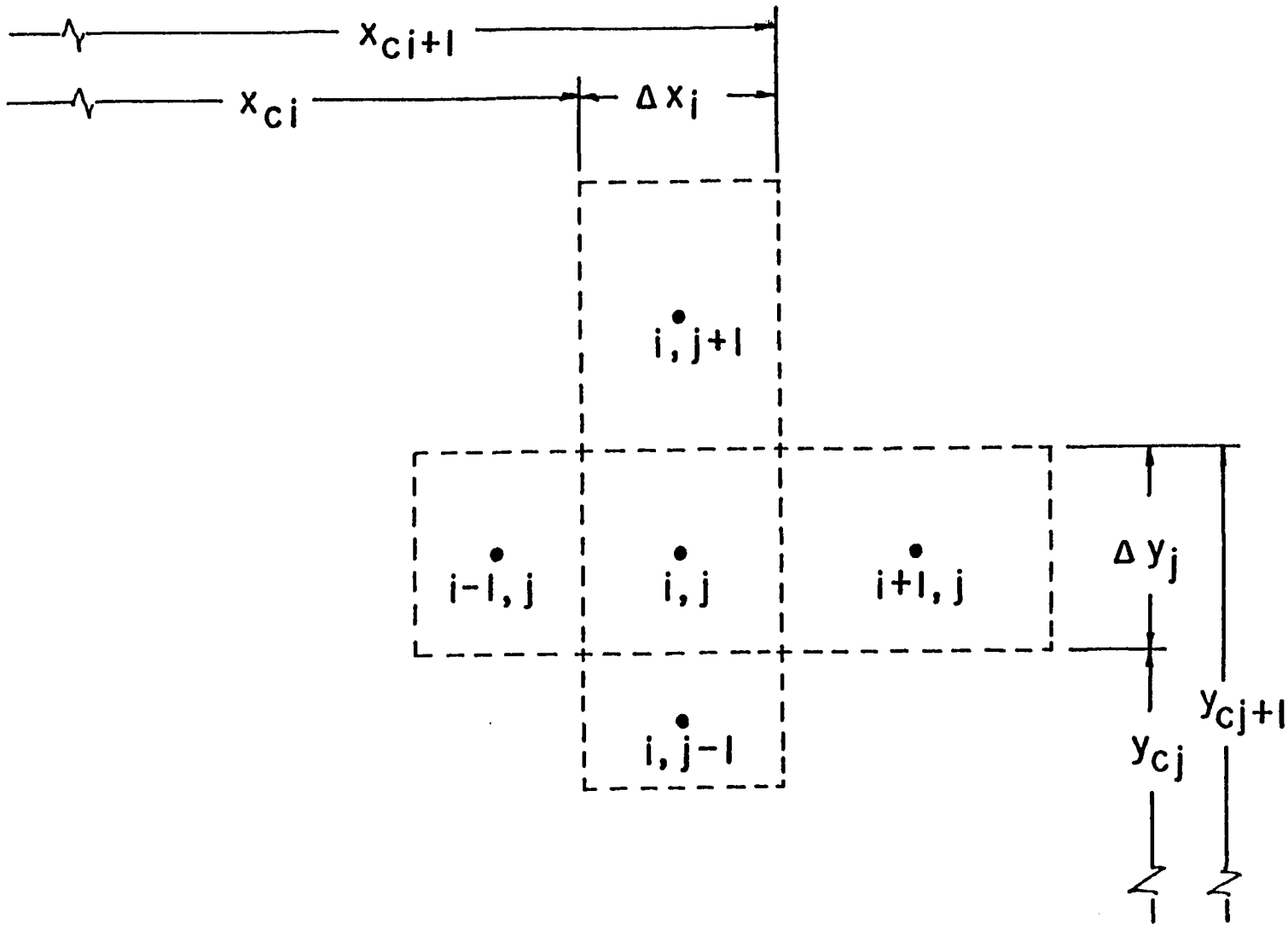

Fig. 3 Diagram of Node Arrangement around Fluid Cells in the Computational Domain

and so on and so forth. Note that the nodes are midway between control faces (dashed lines). For the evaluation of the convective terms in (25), we use an upstream weighted scheme as follows:

$$\int_{y}^{y+\Delta y} (u\omega)_{x+\Delta x}\, dy = [u_{i+1/2,j}\ \omega_{i,j}]\ \Delta y_j \tag{30}$$

Note that the velocity at the right-hand cell face convects vorticity at the upwind node.

When these expressions are assembled into (24) and each term is divided by $\Delta x_i \Delta y_j$, the result is

$$\begin{aligned}\frac{\partial}{\partial t}\omega_{i,j} = {} & \frac{1}{\Delta x_i}\left\{[u_{i-1/2,j}\ \omega_{i-1,j}] - [u_{i+1/2,j}\ \omega_{i,j}]\right\} \\ & + \frac{1}{\Delta y_j}\left\{[v_{i,j-1/2}\ \omega_{i,j-1}] - [v_{i,j+1/2}\ \omega_{i,j}]\right\} \\ & + \frac{2}{Re}\left\{\frac{1}{\Delta x_i}\left[\frac{(\omega_{i+1,j} - \omega_{i,j})}{(\Delta x_i + \Delta x_{i+1})} - \frac{(\omega_{i,j} - \omega_{i-1,j})}{(\Delta x_{i-1} + \Delta x_i)}\right]\right. \\ & \left. + \frac{1}{\Delta y_j}\left[\frac{(\omega_{i,j+1} - \omega_{i,j})}{(\Delta y_{j+1} + \Delta y_i)} - \frac{(\omega_{i,j} - \omega_{i,j-1})}{(\Delta y_{j-1} + \Delta y_j)}\right]\right\}\end{aligned} \tag{31}$$

It remains to integrate (31) with respect to time. We use the explicit method which presumes that the right-hand side of (31) is evaluated at time level t. Next, both sides of (31) are integrated over time interval Δt. Upon rearrangement, one has

$$\omega_{i,j}^{k+1} = \omega_{i,j}^{k}\left\{1-u_{i+1/2,j}^{k}\frac{\Delta t}{\Delta x_i} - v_{i,j+1/2}^{k}\frac{\Delta t}{\Delta y_j} - \frac{2\Delta t}{Re}\left[\frac{1}{\Delta x_i}\left(\frac{1}{\Delta x_i+\Delta x_{i+1}} + \frac{1}{\Delta x_{i-1}+\Delta x_i}\right)\right.\right.$$

$$\left.\left. + \frac{1}{\Delta y_j}\left(\frac{1}{\Delta y_j+\Delta y_{j+1}} + \frac{1}{\Delta y_{j-1}+\Delta y_j}\right)\right]\right\} + \omega_{i+1,j}^{k}\left[\frac{2\Delta t/Re}{\Delta x_i(\Delta x_i+\Delta x_{i+1})}\right]$$

$$+ \omega_{i-1,j}^{k}\left[\frac{u_{i-1/2,j}^{k}}{\Delta x_i} + \frac{2/Re}{\Delta x_i(\Delta x_{i-1}+\Delta x_i)}\right]\Delta t + \omega_{i,j+1}^{k}\left[\frac{2\Delta t/Re}{\Delta y_j(\Delta y_j + \Delta y_{j+1}'')''}\right]$$

$$+ \omega_{i,j-1}^{k}\left[\frac{v_{i,j-1/2}^{k}}{\Delta y_j} + \frac{2/Re}{\Delta y_j(\Delta y_{j-1}+\Delta y_j)}\right]\Delta t \qquad (32)$$

Note that the superscript k now denotes the time level.

For nodes adjacent to solid surfaces, Eqn. (32) must be modified to account for zero normal velocity and the vorticity production. One sets $v_{i,j-1/2} = 0$ or $v_{i,j+1/2} = 0$, depending on whether the cell is bounded below or above by a solid surface. The vorticity production term replaces the diffusion term given by

$$\int_t^{t+\Delta t}\left[\int_x^{x+\Delta x} -\left(\frac{\partial\omega}{\partial y}\right)_y dx\right] dt \qquad (33)$$

where either $y = 0$, $y = S^+$, or $y = S^-$. This entire term is replaced by $-(U_{slip})_{wall}\,\Delta x$ in the case of $y = 0$, and $-(U_{slip})^+_{plate}\,\Delta x$ or $(U_{slip})^-_{plate}\,\Delta x$ in the case of $y = S^+$ or S^-, respectively. Accordingly, one sees that (32) must be modified by adding

$$(\omega_{i,j}^{k} - \omega_{i,j-1}^{k})\; 2\;\Delta t/Re\;\Delta y_j(\Delta y_{j-1} + \Delta y_j)$$

to the right-hand side. This zeros out the flux terms at the lower surface of the control volume. Finally, $-(U_{slip})_{surface}/\Delta y$, is added to the right-hand side [recall that (33) must be divided by $\Delta x_i \Delta y_1$]. A corresponding

modification is made for $y = S^-$, except that now $+(U_{slip})^-_{plate}/\Delta y_1$ is added.

Observe that initially $k = 0$, and the vorticity is everywhere zero. One then has the simple result that adjacent to the top of solid boundaries,

$$\omega_{i,j} = \frac{-(U_{slip})_i}{\Delta y_1} \tag{34}$$

which shows that the initial slip velocity, which after all corresponds to a vortex sheet on the surface, produces the correct amount of free vorticity at the node i,j in time Δt. That is, the initial sheet vortex of strength $(U_{slip})_i$ is broadened by diffusion in time Δt until it fills the whole fluid cell adjacent to the solid surface. Therefore, Δt must be chosen to be the diffusion time for a fluid cell of height Δy. This also ensures the stability of (32), as explained below.

Equation (32) will be stable for sufficiently small Δt such that the coefficient of the $\omega_{i,j}$ term is positive or zero. Adjacent to the solid boundaries, the convective velocities can be neglected, as can the streamwise diffusion of vorticity. Then (32) will be stable provided

$$\left[1 - \frac{2\Delta t}{Re\Delta y_j}\left(\frac{1}{\Delta y_j + \Delta y_{j+1}}\right)\right] \geq 0 \tag{35}$$

This is precisely the statement that Δt be on the order of the time for for vorticity to diffuse a distance Δy. Far from solid surfaces, the incremental heights Δy are greater, and the fluid velocities are important. Then Δt must be sufficiently small that the entire coefficient

of the $\omega^k_{i,j}$ term in (32) be positive or zero. In all cases, the stability critereon was satisfied. It was also verified that the Δy spacing next to solid surfaces was on the order of the diffusion distance for time Δt.

Solution for Stream Function and Velocity Field. As will be explained more fully later, the solution for the perturbation free vorticity, ω', is obtained first. Therefore, the vorticity field is always considered to be known at any given time level.

The solution for the stream function follows from Eqn. (19). For the nodal arrangement shown in Fig. 3, one has by the circulation theorem

$$
\begin{aligned}
-\omega_{i,j}\,\Delta x_i\,\Delta y_j &= \frac{\psi_{i,j+1}-\psi_{i,j}}{.5(\Delta y_j+\Delta y_{j+1})}\,\Delta x_i \\
&- \frac{\psi_{i,j}-\psi_{i+1,j}}{.5(\Delta x_i+\Delta x_{i+1})}\,\Delta y_j - \frac{\psi_{i,j}-\psi_{i,j-1}}{.5(\Delta y_{j-1}+\Delta y_j)}\,\Delta x_i \\
&+ \frac{\psi_{i-1,j}-\psi_{i,j}}{.5(\Delta x_{i-1}+\Delta x_i)}\,\Delta y_j
\end{aligned}
\tag{36}
$$

where the primes on ψ and ω have been omitted for convenience. Upon rearrangement, an equation for $\psi_{i,j-1}$ can be written as follows:

$$
\psi_{i,j-1} = B\,\omega_{i,j} + C\,\psi_{i,j} + D\,\psi_{i,j+1} + E\,\psi_{i+1,j} + F\,\psi_{i-1,j} \tag{37}
$$

where
$$
B = -\frac{\Delta y_j}{2}(\Delta y_{j-1}+\Delta y_j) \tag{38}
$$

$$
C = 1 + \frac{\Delta y_j(\Delta y_{j-1}+\Delta y_j)}{\Delta x_i(\Delta x_i+\Delta x_{i+1})} + \frac{(\Delta y_{j-1}+\Delta y_j)}{(\Delta y_j+\Delta y_{j+1})} + \frac{\Delta y_j(\Delta y_{j-1}+\Delta y_j)}{\Delta x_i(\Delta x_{i-1}+\Delta x_j)} \tag{39}
$$

$$
D = -\frac{(\Delta y_{j-1}+\Delta y_j)}{(\Delta y_j+\Delta y_{j+1})} \tag{40}
$$

$$E = -\frac{\Delta y_j(\Delta y_{j-1}+\Delta y_j)}{\Delta x_i(\Delta x_i+\Delta x_{i+1})} \tag{41}$$

$$F = -\frac{\Delta y_j(\Delta y_{j-1}+\Delta y_j)}{\Delta x_i(\Delta x_{i-1}+\Delta x_i)} \tag{42}$$

The foregoing equation applies at any interior node for which the control volume (dashed lines in Fig. 3) does not lie adjacent to a boundary. A special form must be used for boundary nodes, since the boundary conditions corresponding to Eqns. (20) and (21) and $\psi = 0$ on the wall must be satisfied. The task is to find values corresponding to $\psi_{i-1,j}$ and $\psi_{i+1,j}$ at left- and right-hand boundaries, respectively, as well as values corresponding to $\psi_{i,j+1}$ above the top boundary. The boundary condition at the wall is of a different type and will be discussed subsequently.

Recall that the boundary conditions on the sides and top of the domain are given by Eqn. (20) and (21), where the right-hand sides are considered known. Consider first the left-hand boundary. Let (x_p,y_p) be the node (i-1,j) as shown in Fig. 3. Then

$$\left(\frac{\partial\psi}{\partial x}\right)_{i-1,j} = -v_L \tag{43}$$

and the quantity v_L is known. Now expand ψ in the Taylor series as follows:

$$\psi_{i,j} = \psi_{i-1,j} + \left(\frac{\partial\psi}{\partial x}\right)_{i-1,j}\Delta x + \left(\frac{\partial^2\psi}{\partial x^2}\right)_{i-1,j}\frac{\Delta x^2}{2} + O(\Delta x^3) \tag{44}$$

$$\psi_{i+1,j} = \psi_{i-1,j} + \left(\frac{\partial\psi}{\partial x}\right)_{i-1,j}(2\Delta x) + \left(\frac{\partial^2\psi}{\partial x^2}\right)_{i-1,j}\left(\frac{4\Delta x^2}{2}\right) + O(\Delta x^3) \tag{45}$$

Now eliminate $(\partial^2\psi/\partial x^2)_{i-1,j}$ from the above to get

$$\left(\frac{\partial\psi}{\partial x}\right)_{i-1,j} = \frac{4\psi_{i,j} - \psi_{i+1,j} - 3\psi_{i-1,j}}{2\Delta x} + 0\ (\Delta x^2) \tag{46}$$

Note that we have made use of the fact that adjacent to vertical boundaries we have uniform spacing such that $\Delta x_{i-1} = \Delta x_i = \Delta x_{i+1} = \Delta x$. Now substitute (43) into (46) to get

$$\psi_{i-1,j} = \frac{2\Delta x\ v_L + 4\psi_{i,j} - 4\psi_{i+1,j}}{3} \tag{47}$$

The corresponding expression on the right-hand boundary is

$$\psi_{i+1,j} = \frac{-2\Delta x\ v_R + 4\psi_{i,j} - \psi_{i-1,j}}{3} \tag{48}$$

For the top of the boundary we use the simple first-order scheme. This is necessary due to the solution algorithm adopted to find $\psi_{i,j}$. This will become apparent shortly. One obtains for the top row of nodes

$$\psi_{i,j+1} = \psi_{i,j} + u_T\,\Delta y \tag{49}$$

where u_T is known from the right-hand side of (20) for (x_p, y_p) corresponding to the node (i, j+1).

The enforcement of the boundary condition at the wall is treated next. It is recognized that the wall coincides with the horizontal control-volume face between nodes i, j-1 and i,j. Along this face, $\psi_{i,w}$ must be zero. We first obtain an expression for $\psi_{i,w}$ using the procedure

adopted to derive Eqn. (34). That is, we apply the circulation theorem to a new control volume surrounding node i,1. The height of this control volume is $.75\,\Delta y_1$. The node i,1 is thus a distance of $.5\,\Delta y_1$, above the wall and $.25\,\Delta y_1$ above the lower control face. The upper horizontal control face is a distance of $.5\,\Delta y_1$ above node i,1. The resulting equation differs from (36) in only minor respects. When the result is rearranged to give $\psi_{i,w}$ one obtains

$$\psi_{i,w} = -\left(.375\Delta y_1^2\right)\omega_{i,1} + \left\{1 + \frac{\Delta y_1}{\Delta y_1+\Delta y_2} + .75\Delta y_1^2\left[\frac{1}{\Delta x_i(\Delta x_i+\Delta x_{i+1})}\right.\right.$$

$$\left.\left. + \frac{1}{\Delta x_i(\Delta x_{i-1}+\Delta x_i)}\right]\right\}\psi_{i,1} - \left(\frac{\Delta y_1}{\Delta y_1+\Delta y_2}\right)\psi_{i,2}$$

$$-\left[\frac{.75\,\Delta y_1^2}{\Delta x_i(\Delta x_i+\Delta x_{i+1})}\right]\psi_{i+1,1} - \left[\frac{.75\,\Delta y_1^2}{\Delta x_i(\Delta x_{i-1}+\Delta x_i)}\right]\psi_{i-1,1} \qquad (50)$$

Modifications corresponding to Eqns. (47) and (48) are introduced at the upstream and downstream boundaries. As discussed below, it is required that $\psi_{i,w}$ be zero for all i.

The solution algorithm used to calculate $\psi_{i,j}$ is based on the Stabilized Error Vector Propagation (SEVP) method described in Ref. [4]. The technique is due to Madala [5] and is an extension of the scheme described by Roache [6].

Basically, one begins at the top of the computational domain with j=N. Eqn. (49) is used to replace $\psi_{i,j+1}$ in (37), and expressions (47) and (48) are used adjacent to boundaries. The result is an expression for

$\psi_{i,N-1}$ in terms of $\psi_{i-1,N}$, $\psi_{i,N}$, $\psi_{i+1,N}$ and other known quantities. If values for the stream function along this top row of nodes are given arbitrarily, then one can extend the solution to the next lower row of nodes. This is done until the nodes are reached at the wall, and the stream function there is calculated by (50). Had the initial distribution of ψ along the top row of nodes been correctly given, then $\psi_{i,w}$ given by (50) would be zero. The departure of $\psi_{i,w}$ from zero is a measure of the error, and one can correct the guess for ψ along the top row of nodes according to a systematic procedure. In this way, the correct distribution at j=N can be deduced, and the true values for the stream function over the whole field can be calculated. This is a direct solution method which avoids iteration.

As pointed out in [6], the method fails for large computational grids. That is, any error introduced at some row will eventually grow until the solution becomes meaningless. Therefore, the solution has to be stabilized by subdividing the vertical extent of the domain into subregions or blocks. A direct measure of the error can be obtained, and so subdivisions proceed until the error is acceptable.

The numerical algorithm actually employed is quite complex and is too lengthy to describe here. Details are given in Appendix A.

Having obtained the stream function, it remains to obtain the velocity component, $u = \partial\psi/\partial y$. Since ψ is computed at grid points, the usual expression given by $u = (\psi_{i,j+1} - \psi_{i,j})/.5(\Delta y_j + \Delta y_{j+1})$ gives u which is tangential to the top of a control volume (see Fig. 3). The value

of u desired is perpendicular to vertical control faces between node points. Therefore, a different scheme was devised.

A biquadratic surface was used to interpolate values of ψ between nine node points. The polynomial is of the form

$$\psi = a + b\,x + cy + dxy + ex^2 + fy^2 + g\,x^2y + h\,x\,y^2 + ix^2y^2 \qquad (51)$$

from which

$$u = \partial\psi/\partial y = c + dx + 2fy + gx^2 + 2hxy + 2ix^2y \qquad (52)$$

The nine unknown coefficients (a, b, ..., i) are found in terms of the nine values of ψ at node points (i-1, j-1), (i,j-1), (i+1, j-1), ..., (i+1, j+1). Then u is found from (52). For example, the value of $u_{i-\frac{1}{2},j}$ at the vertical control face between nodes (i-1,j) and (i,j) is found from (52) with $y = .5\,(\Delta y_{j-1} + \Delta y_j)$ and $x = .5\Delta x_{i-1}$. Unfortunately, the coefficients c, d, f, etc. are not given by simple expressions when the node spacing is variable, and therefore, they are not given here. However, they are summarized in Appendix B.

Evaluation of Velocity Field due to Bound and Free Vorticity. The presence of the plate in the flow field means that the domain is not simply connected, and the flow can have a purely irrotational component. As we have seen, this can be handled by the introduction of bound vorticity on the plate. One must calculate the velocity field due to this bound vorticity. The complete expression for u is given by

$$u(x_p,y_p,t) = U_b(y) + \frac{\partial \psi'}{\partial y} + \frac{1}{2\pi}\int_{-1/2}^{1/2} \gamma \left[\frac{S-y_p}{(x-x_p)^2+(S-y_p)^2} + \frac{S+y_p}{(x-x_p)^2+(S+y_p)^2}\right]dx \quad (53)$$

The integral over the plate in the above expression is done numerically. First, polar coordinates are introduced, as discussed earlier (i.e. $x = .5 \cos\theta$). The quantities x_p, y_p and S(=1) are fixed. Next $\gamma \sin\theta$ is replaced by $\hat{\gamma}$ Over any one of the 80 intervals $\Delta\theta_i$, $\hat{\gamma}_i$ is assumed to be constant. For points close to a plate segment, the quantity in brackets in (53) is integrated numerically over the segment using the Gauss quadrature method with 20 Gauss points. For points far removed from the segment, the quantity in brackets is approximated as being constant over a segment. It is evaluated at the midpoint of the segment, and the integral is this value multiplied by $\Delta\theta_i$. Following this procedure for any fluid point (x_p, y_p), one obtains a sum of 80 contributions for the 80 values of γ_i. Each contribution is a value of γ_i multiplied by a geometrical coefficient, which is constant for all time. Therefore, these 80 coefficients for each fluid point were calculated once and stored.

Integrals over the field of free vorticity exist in Eqns. (14), (15), (16), (17), and (20) and (21) for (x_p,y_p) on the right, left, and top boundaries of the computational domain. Recall that these latter expressions are needed to find v_R, v_L and u_T for use in (47), (48), and (49). In all cases the basic idea is the same. Over any fluid cell, $\omega_{i,j}$ is considered to be constant and is factored outside the integral. The kernel functions are then integrated over cells $\Delta x_i\ \Delta y_j$. Since each cell

is rectangular, it is divided into 40 vertical strips, which are centered on the 40 Gauss points for the interval Δx_i. Each vertical strip is treated as being of infinitesimal width, and the integral over Δy_j is carried out exactly (see Ref. [7] for more details). These results are then multiplied by the corresponding dx_i, and the results are summed according to the weighting scheme given in the Gauss quadrature formula. This gives one geometrical coefficient for the cell $\Delta x_i \Delta y_j$ and a point (x_p, y_p). When the cell is far from the point, that is $r \geq 10\,(\Delta x_i, \Delta y_j)^{1/2}$, then the kernel is treated as constant. The integral is then the kernel evaluated at the center of the cell multiplied by the cell area.

In this way, geometrical coefficients are computed for each fluid cell and any given point (x_p, y_p). The results are calculated once and stored for each point.

In principle, the y-component of velocity could be found from an equation similar to Eqn. (53). It is more expedient to obtain it from the continuity equation, once the u velocity component is found. That is, Eqn. (8) is integrated with respect to y and then with respect to x. Thus

$$\int_0^y u(x+\Delta x, y)\,dy - \int_0^y u(x,y)\,dy + \int_x^{x+\Delta x} v(x,y)\,dx = 0 \qquad (54)$$

where the wall condition $v(0)=0$ has been applied. To second order, the integrals can be approximated as follows:

$$\sum_{j=1}^{n} u(x+\Delta x_i, y_j)\Delta y_j - \sum_{j=1}^{n} u(x, y_j)\Delta y_j + v(x+\frac{\Delta x_i}{2}, y_n)\Delta x_i = 0 \qquad (55)$$

The indices i and j are as shown in Fig. 3. Upon rearrangement, one has with different notation

$$v_{i,n+1/2} = -\frac{\Delta y_j}{\Delta x_i} \sum_{j=1}^{n} (u_{i+1/2,j} - u_{i-1/2,j}) \qquad (56)$$

where n is the number of fluid cells above the wall in the vertical direction. Note that (56) is not applied to fluid cells which are bounded on the top by the plate. The transverse velocity there is already forced to zero by the bound vorticity distributed along the plate.

A final detail has yet to be mentioned. This pertains to the calculation of the diffusive flow of free vorticity from the top and bottom of the plate into the surrounding fluid. This involves the application of Eqns. (16), (17), and (18).

The apparent slip velocity is found at each of 80 points on the plate, and yet there are only twenty fluid cells which are in contact with fluid on either the top or bottom of the plate. Therefore, the local slip velocity was integrated over each cell face, using Simpson's rule, in order to get an effective slip velocity for each fluid cell. This was not required on the wall since a local slip velocity was calculated at the center of each cell face in contact with the wall.

Numerical Parameters. Most of the gross features of the computational grid are apparent from Fig. 2. There are 11,200 fluid cells

in all. There are 80 cells in the vertical direction and 140 in the streamwise direction.

The cell dimensions are first determined on the plate. There are 20 cells which span the unit plate length. First, 20 points are located over the unit interval according to the scheme in the 20-point Gauss quadrature formula. Control faces of fluid cells are then located midway between these points. This produces 20 cells with a size distribution which is symmetrical about $x = 0$, and which allows the clustering of cells near the plate leading and trailing edges. The same distribution is used in the fluid region above and below the plate, as well as ahead of and behind the leading and trailing edges. Outside the range $-1 \leq x \leq +1$, the spacing is uniform and equal to $\Delta x = 0.12$ until $x = \pm 4.0$. For $x > 4.0$, the horizontal spacing is 0.16.

The unit length between the plate and wall has the same distribution of cells as that over the plate. Above the plate, cell dimensions expand in a fashion symmetrical to those below the plate, but for five cells only (rather than the usual ten). Beyond this point, the spacing is uniform and equal to $\Delta y = .0517$.

The maximum time step was selected to be $\Delta t = .01$. Recall that this means that a fluid particle moving with the free-stream velocity will travel one plate length in 100 time increments. Provisions were made to reduce Δt, if necessary, in order to render the calculations stable. The reduction was always 10% of the current Δt. The Δt was never smaller than .0081.

Model for the Large-Scale Eddies

A total of eleven different eddies was specified to enter the upstream flow boundary over the total time interval t = 10. For t > 10, the eddy pattern repeats itself.

A schematic of the eddy pattern is shown in Fig. 4. The initial vorticity strengths are shown for each eddy. One can envision that this pattern moves to the right undistorted with the free-stream velocity, U_∞. The computational domain is just to the right. Therefore, this pattern can be supposed to exist for a distance of ten plate lengths upstream of the inflow boundary, and it moves as an ensemble until the outline of an eddy just touches the inflow boundary. After this point in time, the vorticity of the eddy, plus the background flow, convects into the domain with the local fluid velocity.

Since the grid is rectangular and the eddy is taken to be circular, its shape could only be approximated. An example of this is shown for the third eddy in Fig. 5. The eddy spans vertical layers $j = 7$ to $j = 17$. The diameter is 0.7245, and the center is at $y = .576$ and $\ell_c = 2.30$.

As seen in Fig. 5, horizontal grid lines intersect the circular outline of the eddy (dashed circle), thereby defining the sector of a circle. The difference between the areas of two sectors formed by adjacent grid lines corresponds to the area of a horizontal strip intersecting with the circle. A rectangle of equal area can then be formed by dividing this latter area by the height of a strip. In this way, a stair-step outline of the eddy is produced.

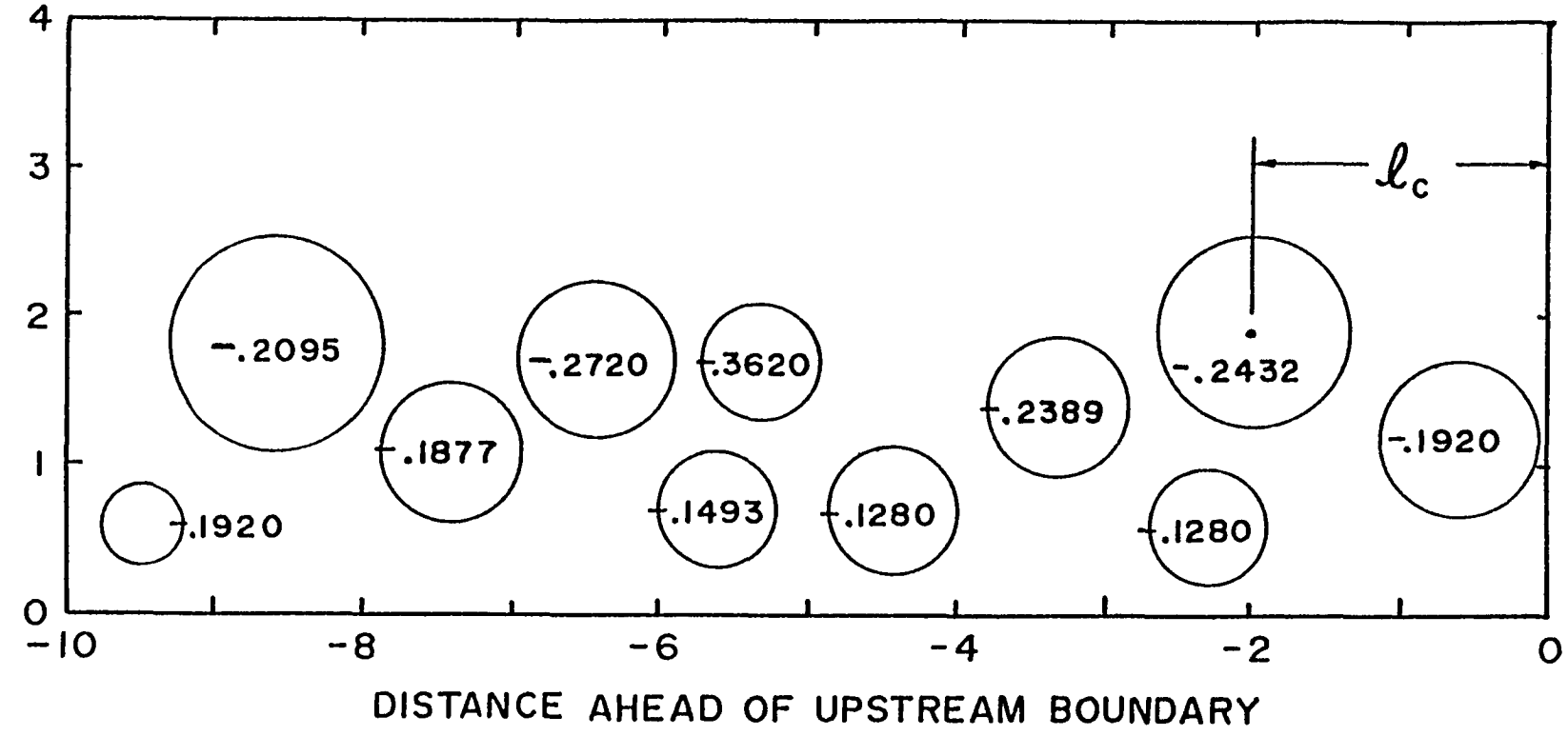

Fig. 4 Schematic Diagram of Eddy Pattern Introduced at Upstream Boundary

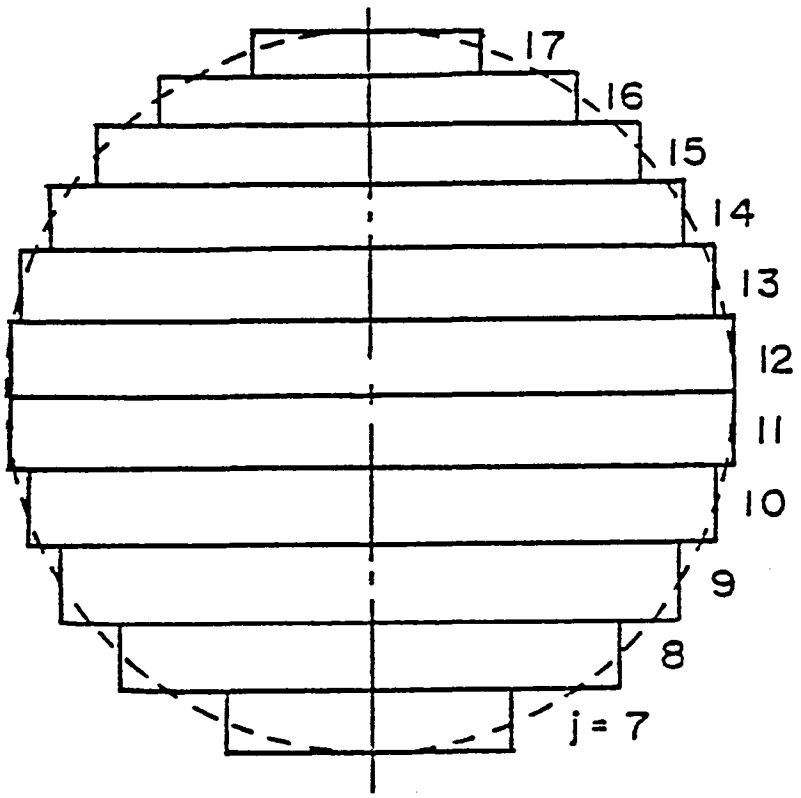

Fig. 5 Representation of Circular Eddy by Rectangular Grid

The initial vorticity of each eddy is preassigned. The vorticity is assumed to be uniformly distributed over its area. The vorticity strength is chosen so that the velocity induced at the wall by a single eddy is no more than 2% of the free stream velocity. The nondimensional eddy strength varies from .128 to .362. To obtain the maximum perturbation velocity due to a single eddy, one divides the eddy vorticity by 4.

The perturbation vorticity of the eddy is added to the background vorticity at the upstream boundary. This then defines the vorticity which enters an upstream control volume at any elevation, j. Vorticity enters according to a certain time schedule. Because the eddies are assumed to move toward the upstream boundary at uniform velocity U_∞, and this velocity is used to nondimensionalize the time, their nondimensional locations ahead of the upstream boundary are equivalent to delay times. For example, suppose j = 10, and we are concerned with vorticity entering the grid from eddy #3 (shown in Fig. 5). For j = 10, the length of the equivalent rectangular area is 0.6865. The center of the eddy is at $\ell_c = 2.30$. Therefore, vorticity from this eddy is added to the background vorticity at j = 10 for $t_1 \leq t \leq t_2$, where $t_1 = 2.3 - 0.6865/2$ and $t_2 = 2.3 + 0.6865/2$.

Computational Procedure

The calculations start from an initial state of rest. We envision that the flow is started impulsively with the background velocity field. The coherent eddies do not enter the upstream boundary until after a finite delay time.

The flow is initiated at $t = 0^+$. Immediately, there is an apparent velocity slip along the plate given by $(U_{slip})^+_{plate} = (U_{slip})^-_{plate} = U_b(y=1)$. These apparent slip velocities form surface boundary conditions along the plate for the vorticity transport equation. As discussed in connection with Eqn. (32), the vorticity in the fluid cells adjacent to the plate is now non-zero and is given by $\pm U_b(y=1)$ depending on whether the cell is above (minus sign) or below (plus sign) the plate. The vorticity throughout the entire field is calculated. A small lateral diffusion of background vorticity takes place.

Note that the vorticity obtained in this first step includes the background plus perturbation vorticity. This will be the case for all calculations of the vorticity field. Also, the vorticity is convected by the total velocity (background plus perturbation).

To obtain the perturbation velocities, however, we need only the perturbation vorticity, ω'. This is obtained next by subtracting $\Omega_b(y)$ from the vorticity field. Now the boundary value for the perturbation stream function can be obtained from Eqns. (20) and (21), following which ψ' can be calculated. One contribution to the x-component of perturbation velocity is next obtained from $\partial\psi'/\partial y$ everywhere in the field.

It remains to calculate the perturbation velocities due to the bound vorticity, γ, and the apparent slip velocities along the wall and plate surfaces. First, ω' is used to calculate the right-hand side of Eqn. (14), after which $\gamma(x_p)$ is obtained numerically from this integral equation. Finally, the contribution to the x-component of velocity due to

γ is obtained from the second integral in (12). Recall that the first integral has been replaced by $\partial\psi'/\partial y$. Now that both contributions to the perturbation velocity in the x-direction are known, these are added and the y-component of perturbation velocities is calculated from the continuity equation.

The apparent slip velocities at solid surfaces are obtained from Eqns. (15), (16), and (17). These now form the boundary conditions for the vorticity transport equation.

The computational cycle is now repeated. With each integration of the vorticity transport equation, the conditions at the upstream boundary are checked to see if eddy vorticity is ready to enter the grid. If not, then $\Omega_b(y)$ is convected in. Otherwise, the eddy vorticity is added to $\Omega_b(y)$ and the total is convected in.

IV. RESULTS AND DISCUSSION

All computations were performed on the CDC CYBER 203 at the Langley Research Center. The computer jobs were submitted by remote batch from the Aerospace and Mechanical Engineering Department of the University of Arizona. The total central processing time for the results shown was 2.64 hours.

The primary results are presented in the form of vorticity contour plots. In addition, a sense of the flow development is provided by figures obtained using the marker and cell technique developed by Harlow and co-workers at the Los Alamos Scientific Laboratories (see Ref. [8]).

The plots are grouped at the end of this section and are given after each 160 time steps, which corresponds to a dimensionless time interval of approximately 1.30. The first plot in each series shows contours of constant perturbation vorticity. This is the vorticity obtained after the contribution from the Blasius velocity profile has been substracted out. Contours are shown for the following values of perturbation vorticity, -.05, -.10, -.20, -.25, -.30, -.50, -1.00, + .50, +1.00. Following each vorticity plot is the flow pattern for the same time obtained with the marker and cell flow-visualization technique. It is emphasized that markers and cells were used only to help visualize the flow development after the complete flow field was obtained from the governing equations given in Chapter III.

The flow is started impulsively from an initial state of rest. One can see in Figs. 1 and 2 that the wake formed by the plate is developing at the same time that the vortical flow introduced at the upstream boundary ($x = -4.0$) is proceeding toward the leading edge of the plate. In Fig. 3, the eddies are just reaching the leading edge of the plate. Four eddies seem to be visible. Secondary vorticity is also being generated on the wall. The region close to the wall ahead of the plate contains positive perturbation vorticity, whereas that region below the plate contains negative perturbation vorticity. Although not shown on the figures, the wall region behind the plate contains slightly positive perturbation vorticity for a large extent behind the trailing edge.

The regions of positive perturbation vorticity near the wall act to reduce the wall skin friction, since it combines with the negative vorticity of the background flow to produce a smaller velocity gradient. This indicates that there is an unfavorable (positive) pressure gradient at the wall ahead of and behind the plate. Directly below the plate on the wall there is a favorable (negative) pressure gradient. Clearly, the flow is accelerated as it flows between the wall and plate, but it is retarded ahead of and behind the plate. The local acceleration is caused by the thickening boundary layer on the plate which acts to restrict the flow area between it and the wall.

The developing wake and flow perturbation ahead of the plate is also visible in Fig. 8A. Initially, all the flow markers were arranged uniformly over the flow field.

At the upstream boundary, new markers are introduced at a constant rate. This simulates hydrogen bubbles released uniformly from a wire placed across the flow. Because the fluid in the boundary layer ($y < 2.0$) moves more slowly than the outer flow, the markers tend to bunch up near the wall. One can also see that the particles appear to follow a wavy path ahead of the plate. This is because they follow the rotary motion due to the eddies.

At an intermediate time of $t = 8.14$ shown in Figs. 11 and 11A, the eddies have merged with the boundary layers on the plate. Note that the perturbation vorticity of the eddies and wake has traveled approximately eight plate lengths, which is in accord with the elapsed time. The vorticity does not appear to penetrate the region directly below the plate, although it is prevalent below the elevation of the plate in the upstream region. This is probably due to the fact that the positive vorticity of the boundary layer on the underneath side of the plate is much stronger than the eddy vorticity. Thus when they merge, they combine to give a net positive vorticity. The vorticities of the eddies and boundary layer are of the same negative sign above the plate.

Note also in Figs. 11 and 11A that there is a fine-scale eddy pattern in the far-wake region behind the plate. Furthermore, the negative vorticity adjacent to the wall directly below the plate has disappeared (compare with Fig. 9). This indicates that the enhanced skin friction there at earlier times has been reduced, as has the negative pressure gradient. Probably more of the flow is passing over the plate rather than between it and the wall.

For $t > 8.14$, only vorticity plots are given. The overall pattern follows that at earlier times. It is interesting that at $t = 10.73$ and 12.03 (Figs. 13 and 14), the vortical pattern characteristic of "cat eyes" is swept over the leading edge of the plate with little distortion. However, at the last time shown of $t = 14.61$, the pattern is completely obscured. Clearly, the plate is acting to break up the eddies at the same time that it is preventing them from penetrating the region close to the wall.

It appears from these computed results that the basic mechanism described by Corke, Nagib, and Guezennec [1] is correct. The plate prevents the large scale eddy from penetrating the wall region below and behind the plate. The strong wake produced by the plate blocks vertical excursions of high speed potential fluid into the boundary layer. Thus the vortical wake behind the plate is very straight and parallel to the wall. The eddies so prevalent ahead of the plate do not persist behind the plate. There does not appear to be a mechanism for their reforming into coherent structures. They seem simply to merge with the plate boundary layers.

Before concluding this section, it is of interest to examine the time development of the drag on the system. This was computed at each time step from the momentum integral relationship. The contribution to the drag from the pressure field was neglected. The vertical flow boundary on the upstream side of the control volume used in the momentum balance was located at $x = -3.4$, That on the downstream side was located at $x = +11.2$. The drag force per unit of span is divided by the horizontal length of the control volume (14.6) to get the drag coefficient plotted in Fig. 17.

The drag coefficient is of limited quantitative value since it is not known what would be the drag if the plate were absent. However, some of the features do appear to be correlated with the actions of the eddies.

There are a number of sharp peaks in the drag curve. These occur at approximately $t = 1.3, 2.5, 4.2$, etc. It appears that these peaks are associated with the arrival of an eddy core at the upstream boundary of the momentum control volume. Since the eddy pattern repeats itself for $t > 10$, the peaks at $t = 11.3$ and 12.7 appear to be repeats of those occurring at $t = 1.3$ and 2.5, although they occur at a higher level.

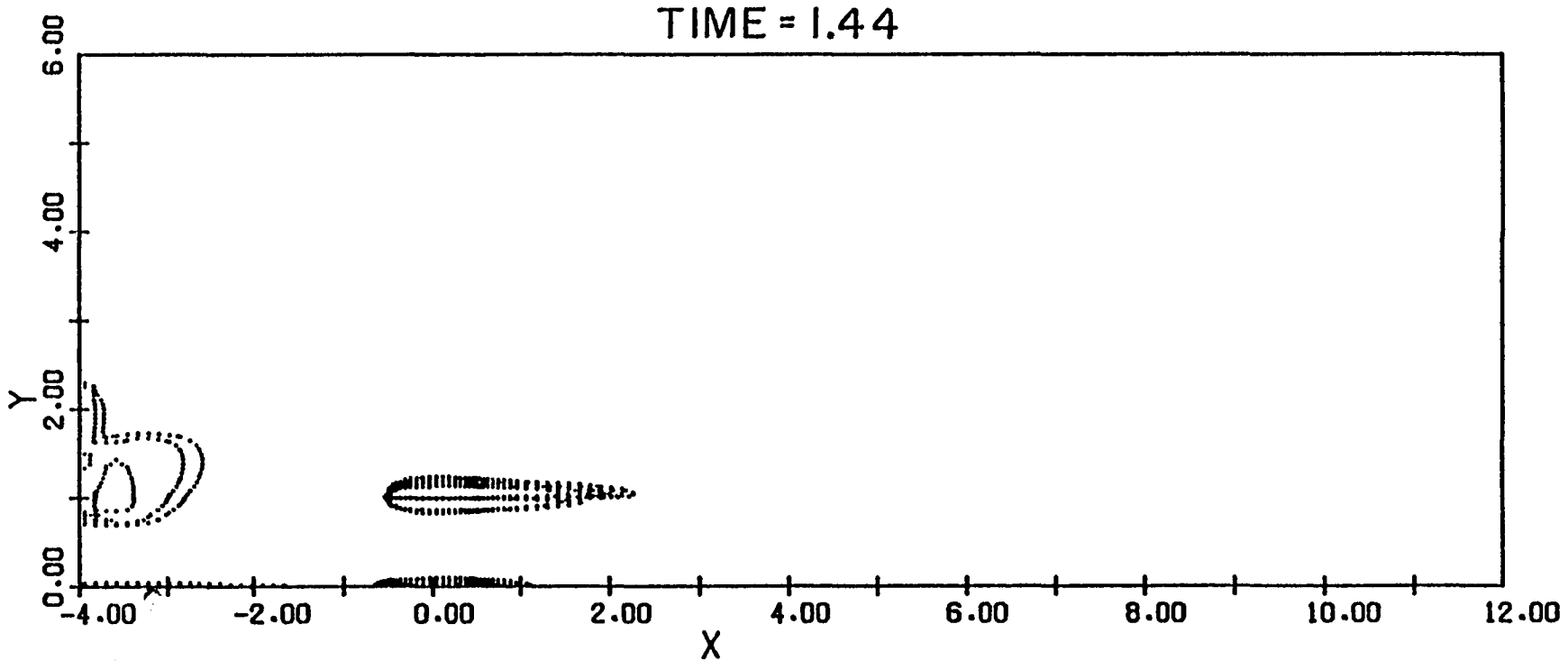

Fig. 6 Contours of Constant Perturbation Vorticity.
t = 1.44

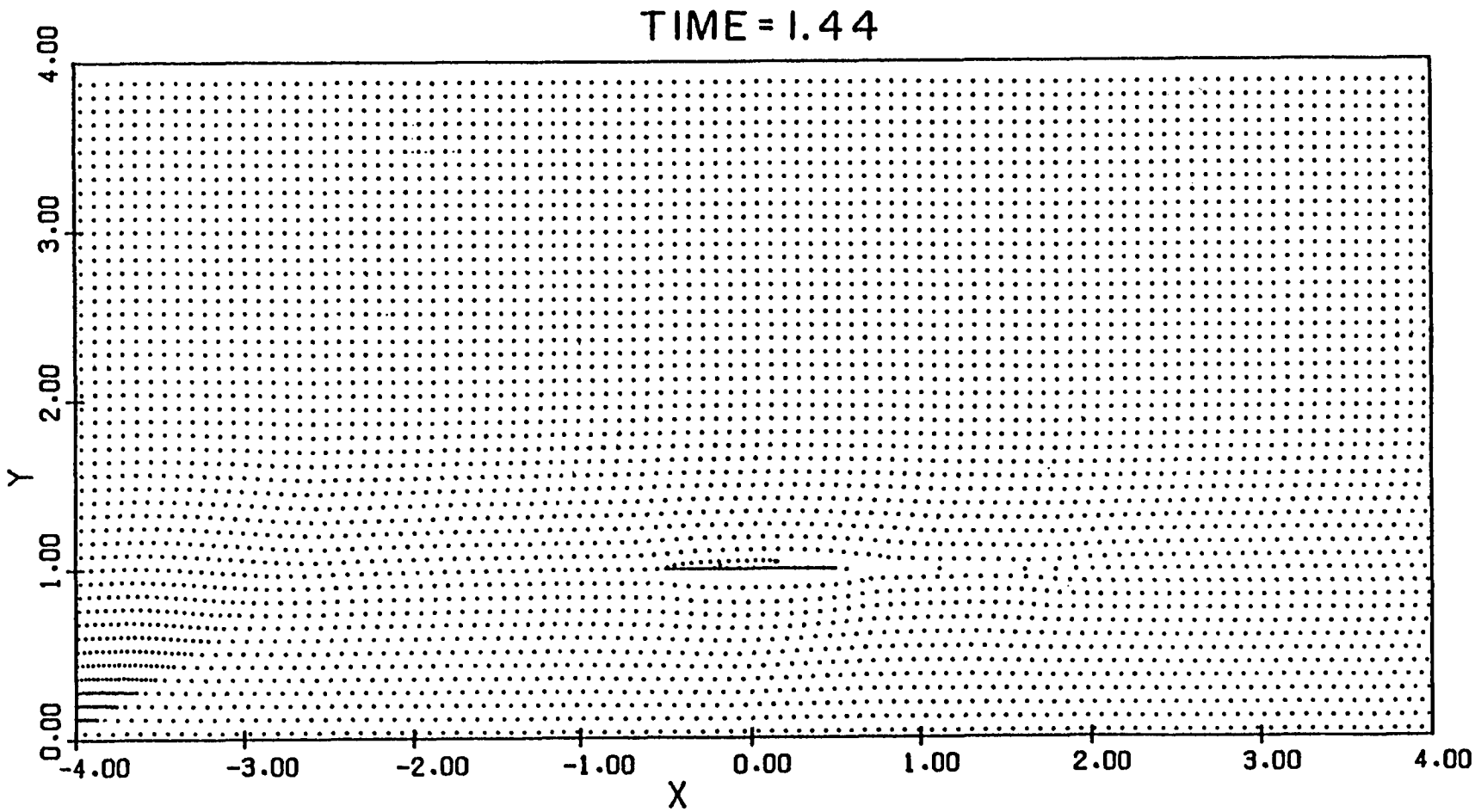

Fig. 6a Marker Particles for t = 1.44

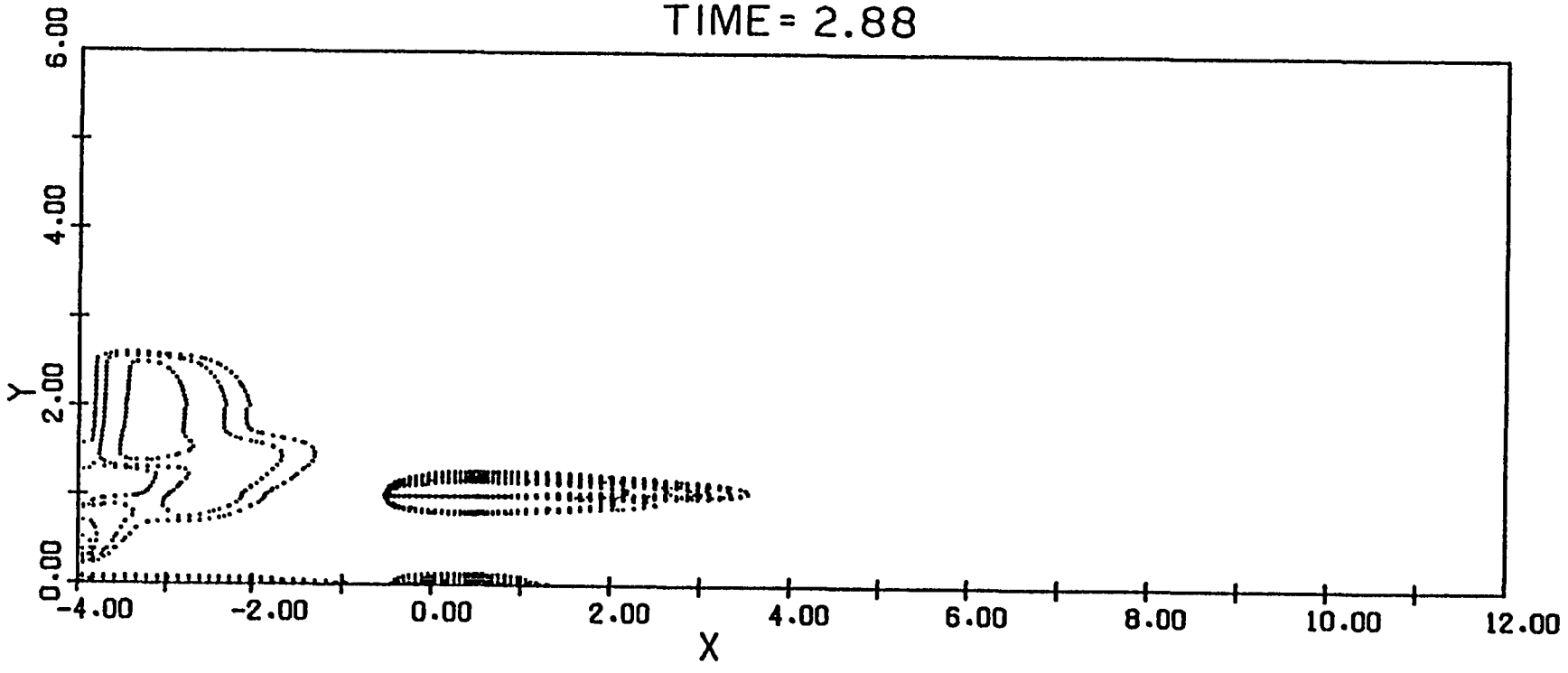

Fig. 7 Contours of Constant Perturbation Vorticity.
t = 2.88

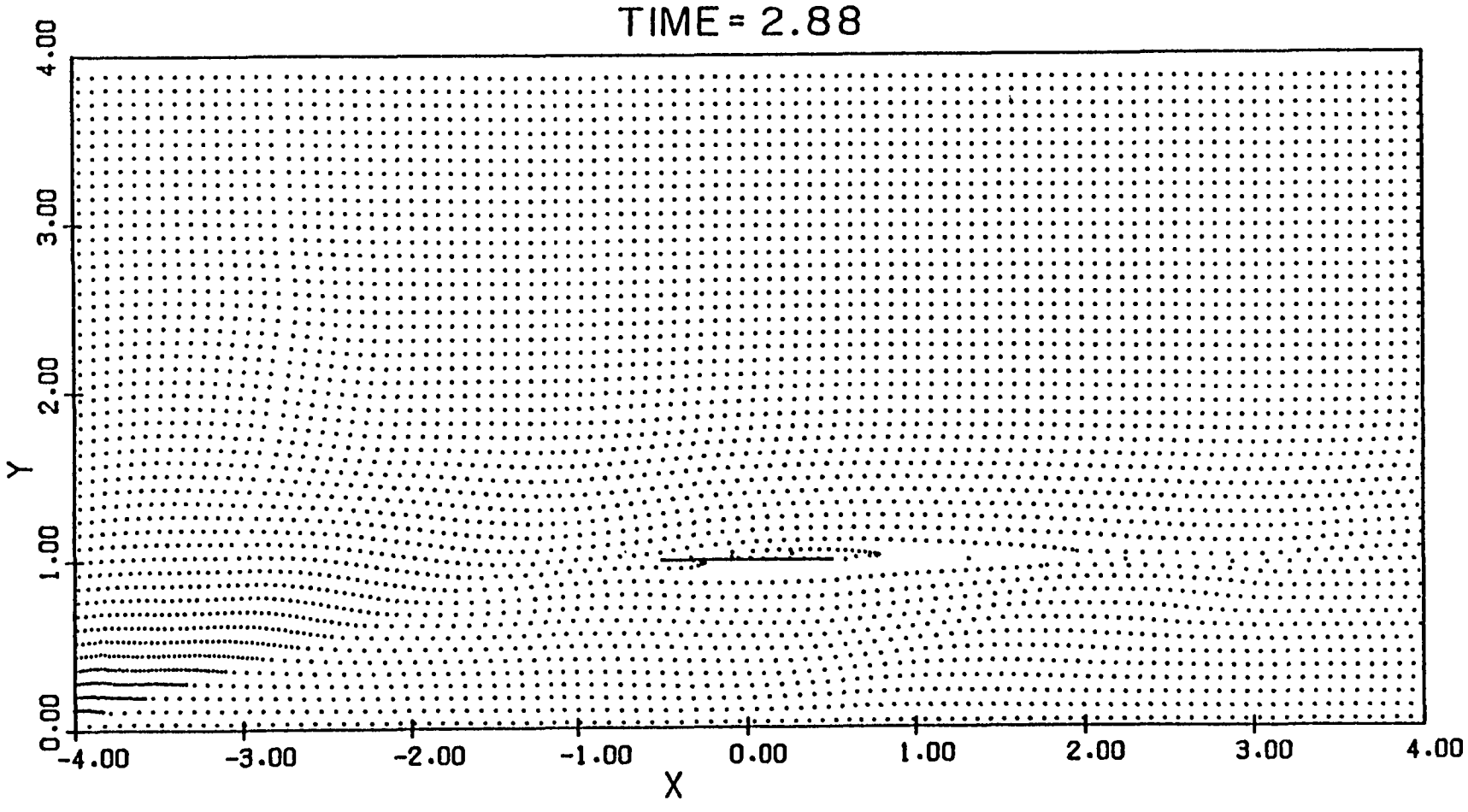

Fig. 7a Marker Particles for t = 2.88

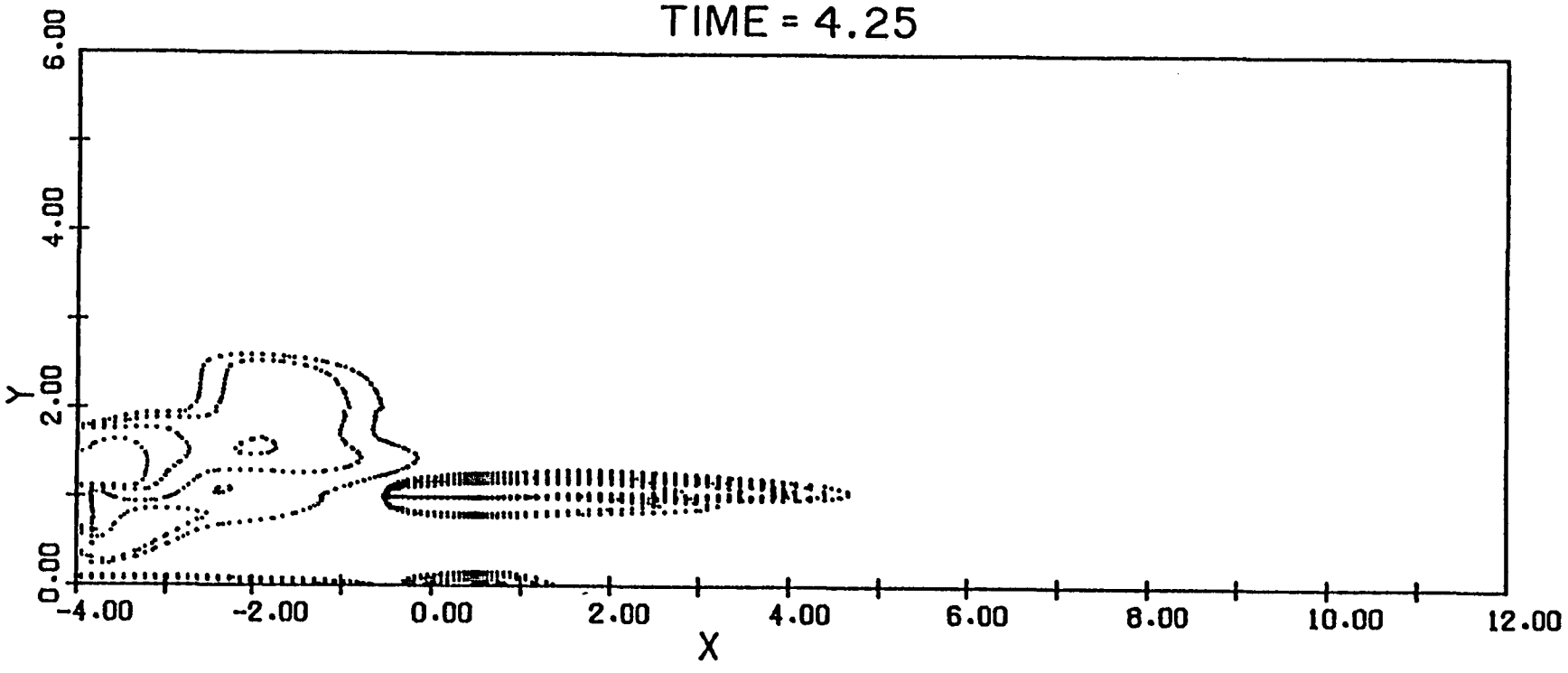

Fig. 8 Contours of Constant Perturbation Vorticity.
t = 4.25

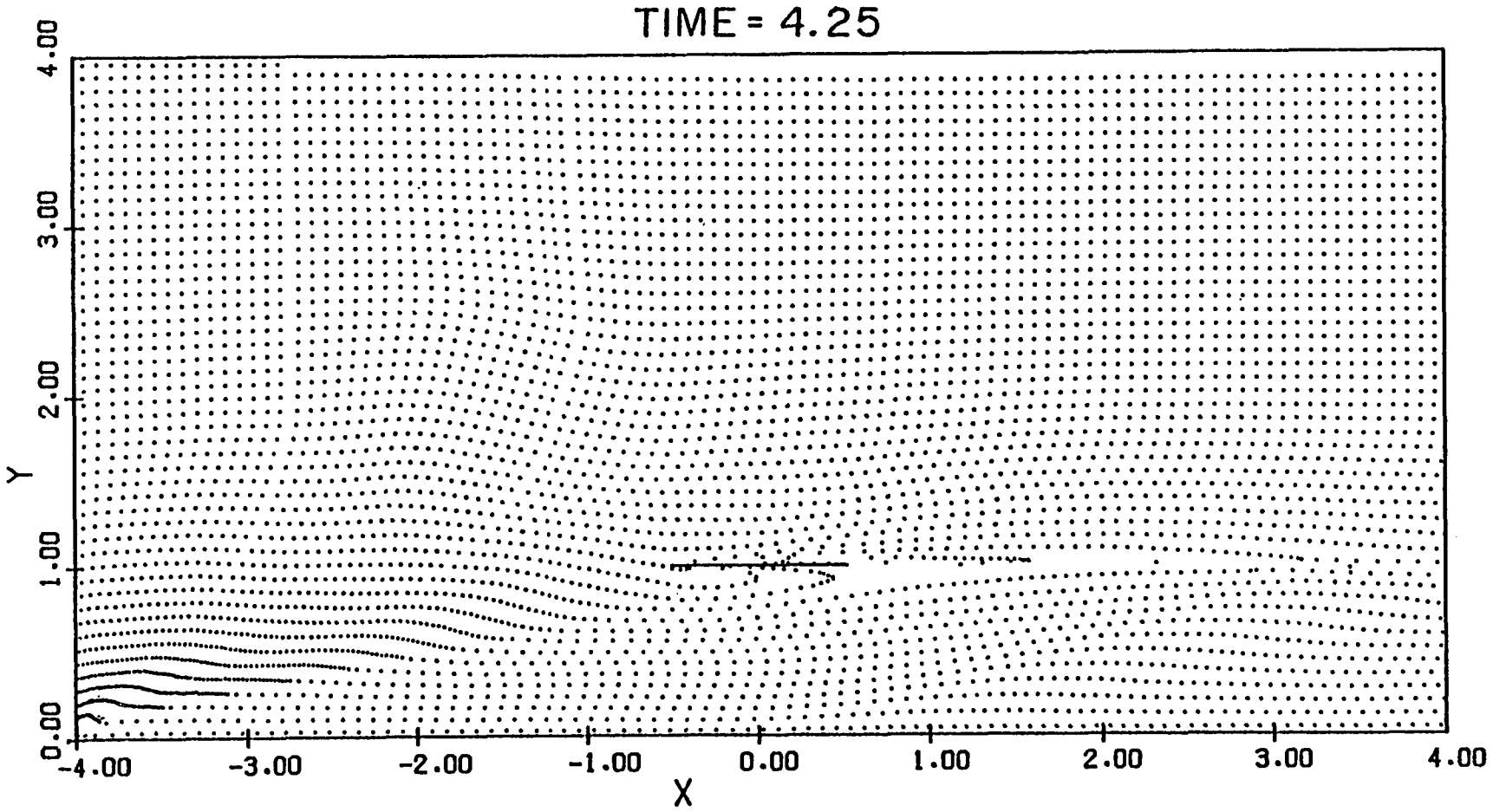

Fig. 8a Marker Particles for t = 4.25

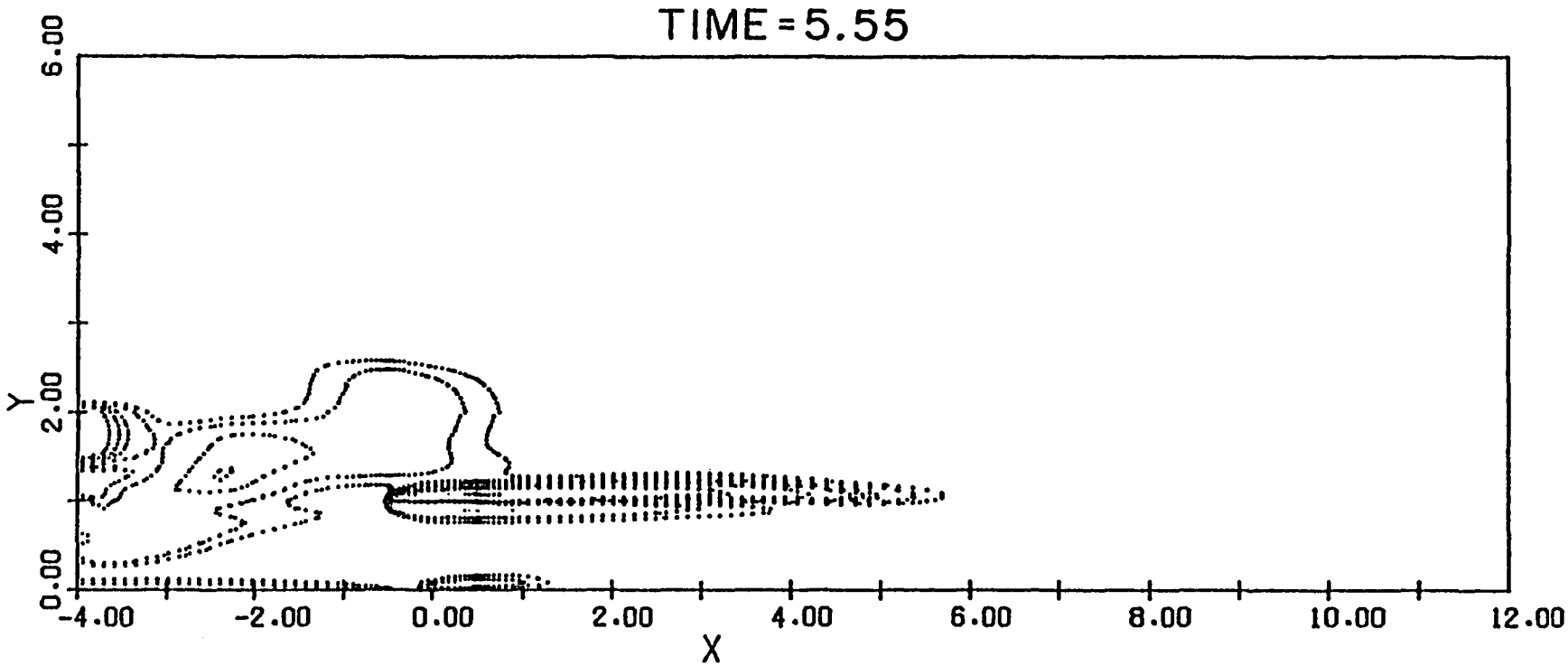

Fig. 9 Contours of Constant Perturbation Vorticity.
t = 5.55

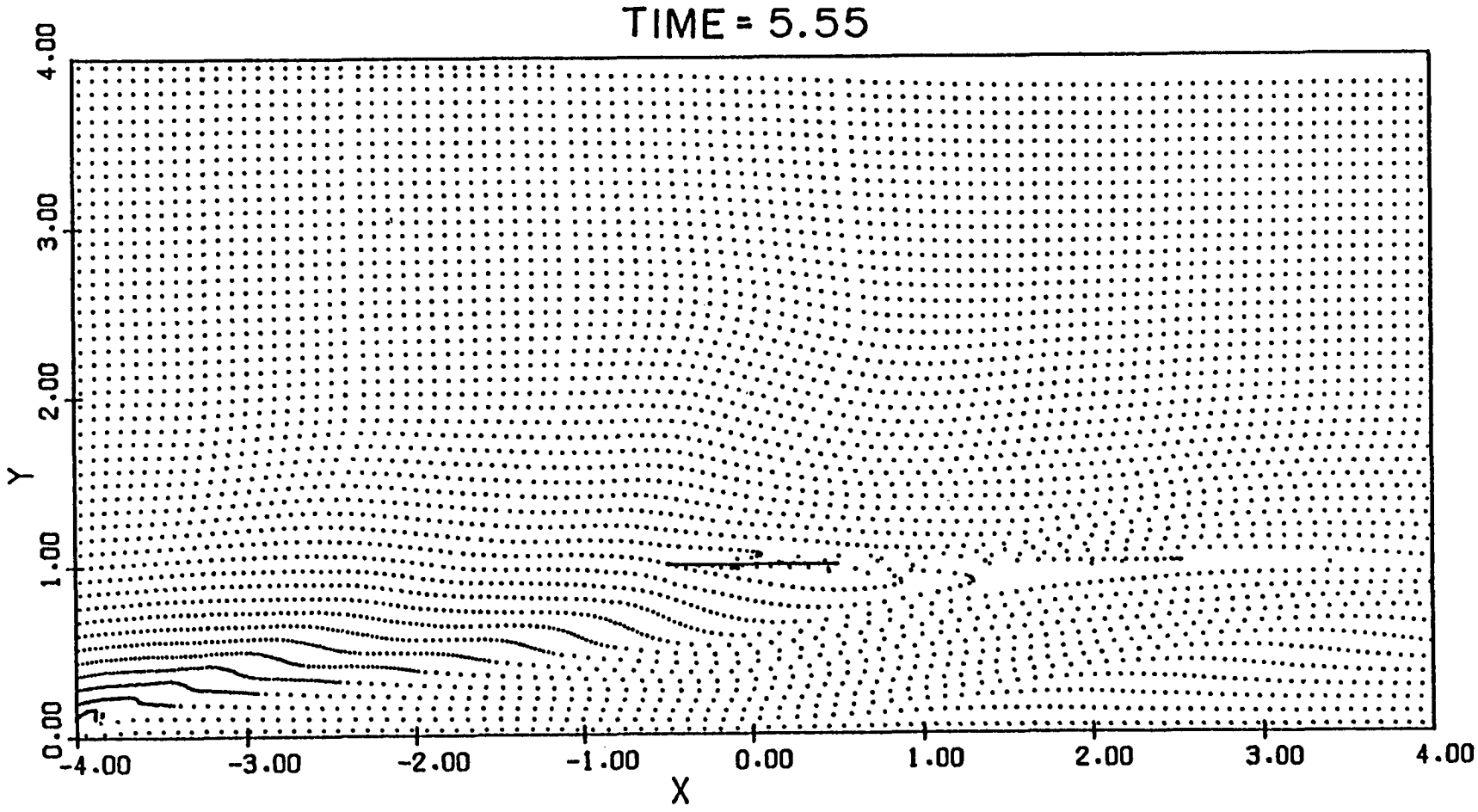

Fig. 9a Marker Particles for t = 5.55

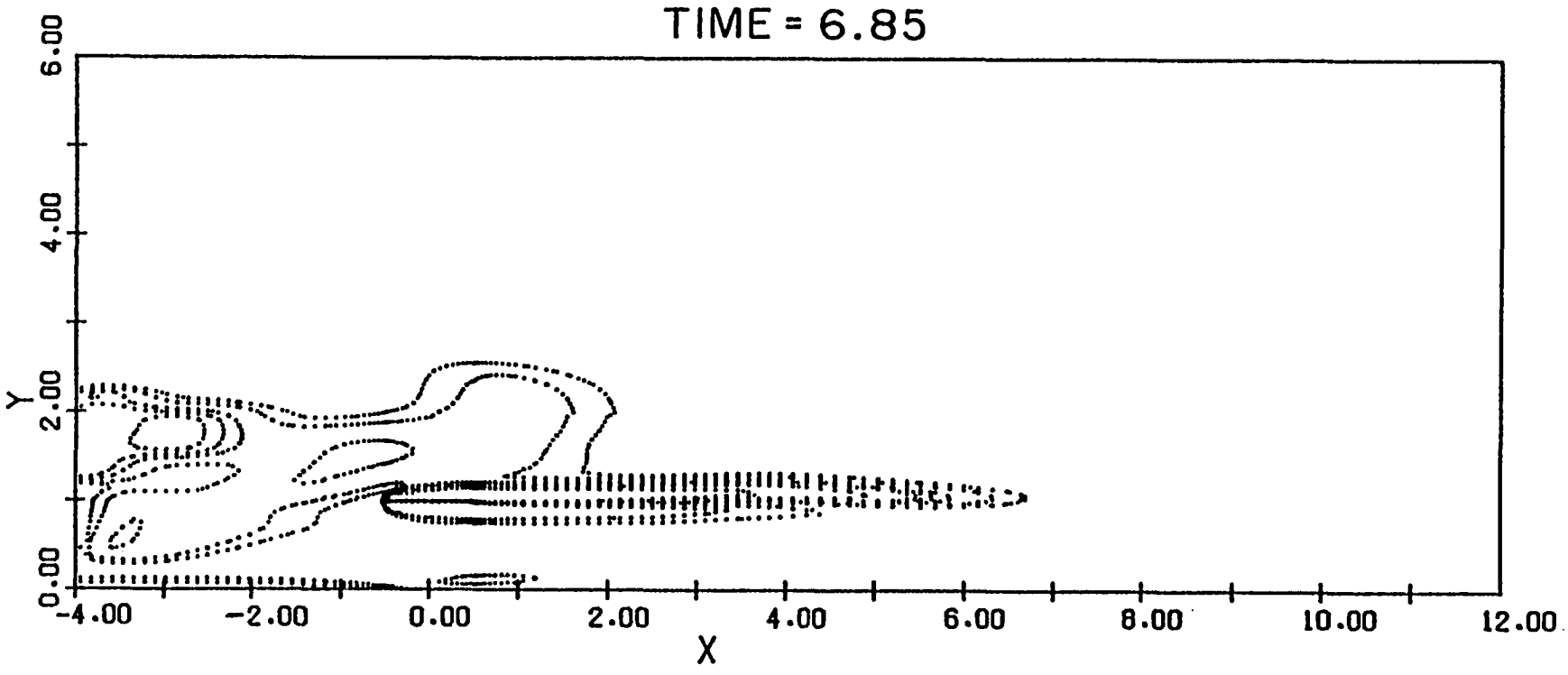

Fig. 10 Contours of Constant Perturbation Vorticity.
t = 6.85

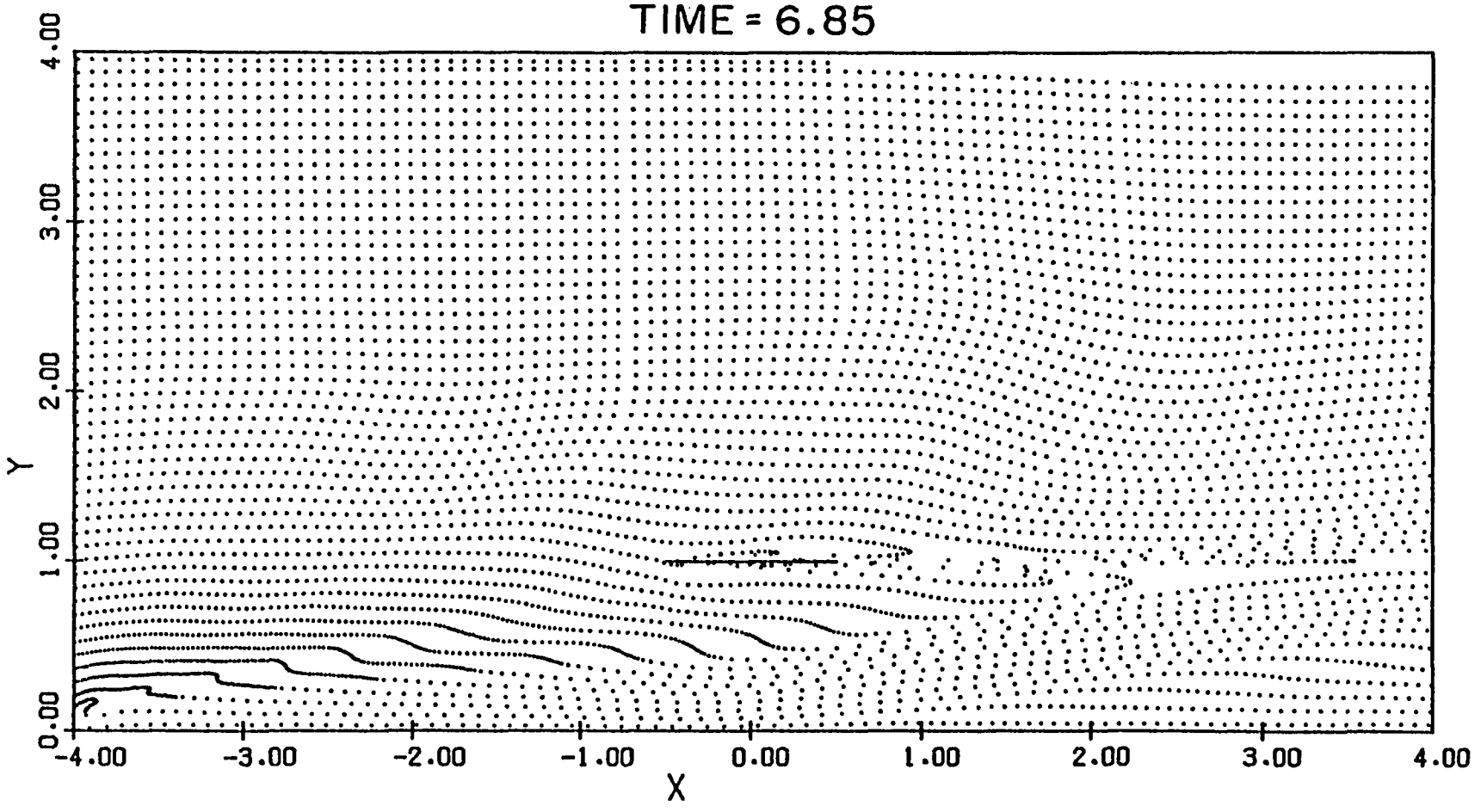

Fig. 10a Marker Particles for t = 6.85

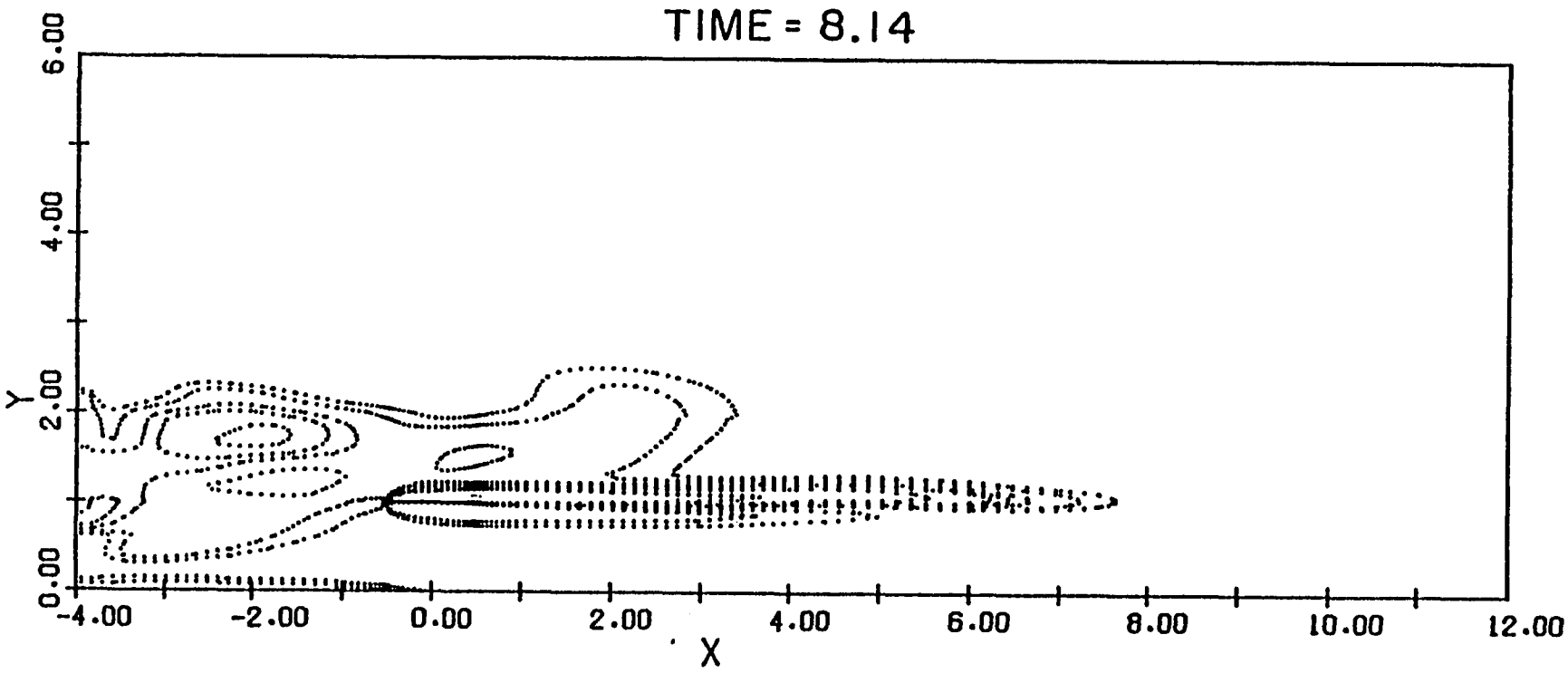

Fig. 11 Contours of Constant Perturbation Vorticity.
t = 8.14

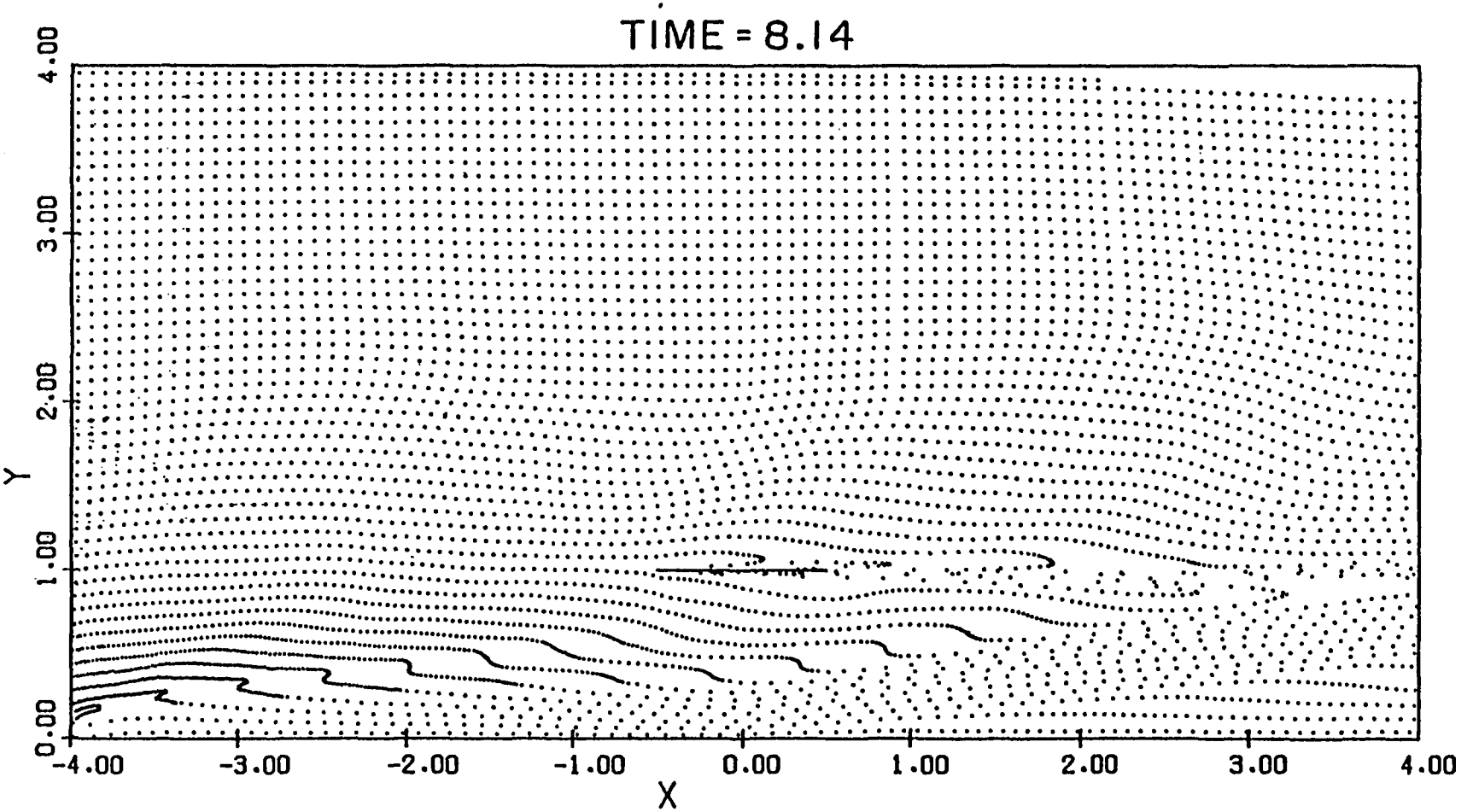

Fig. 11a Marker Particles for t = 8.14

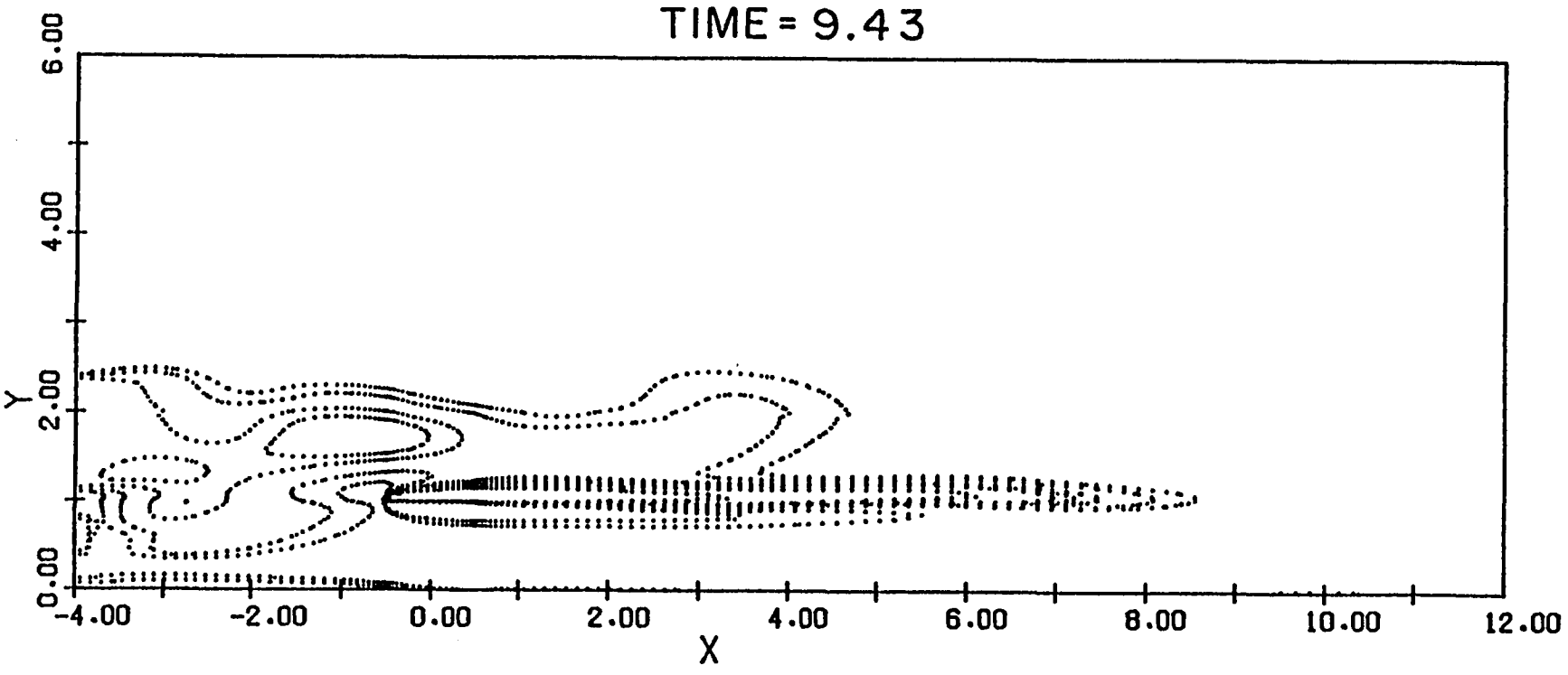

Fig. 12 Contours of Constant Perturbation Vorticity.
t = 9.43

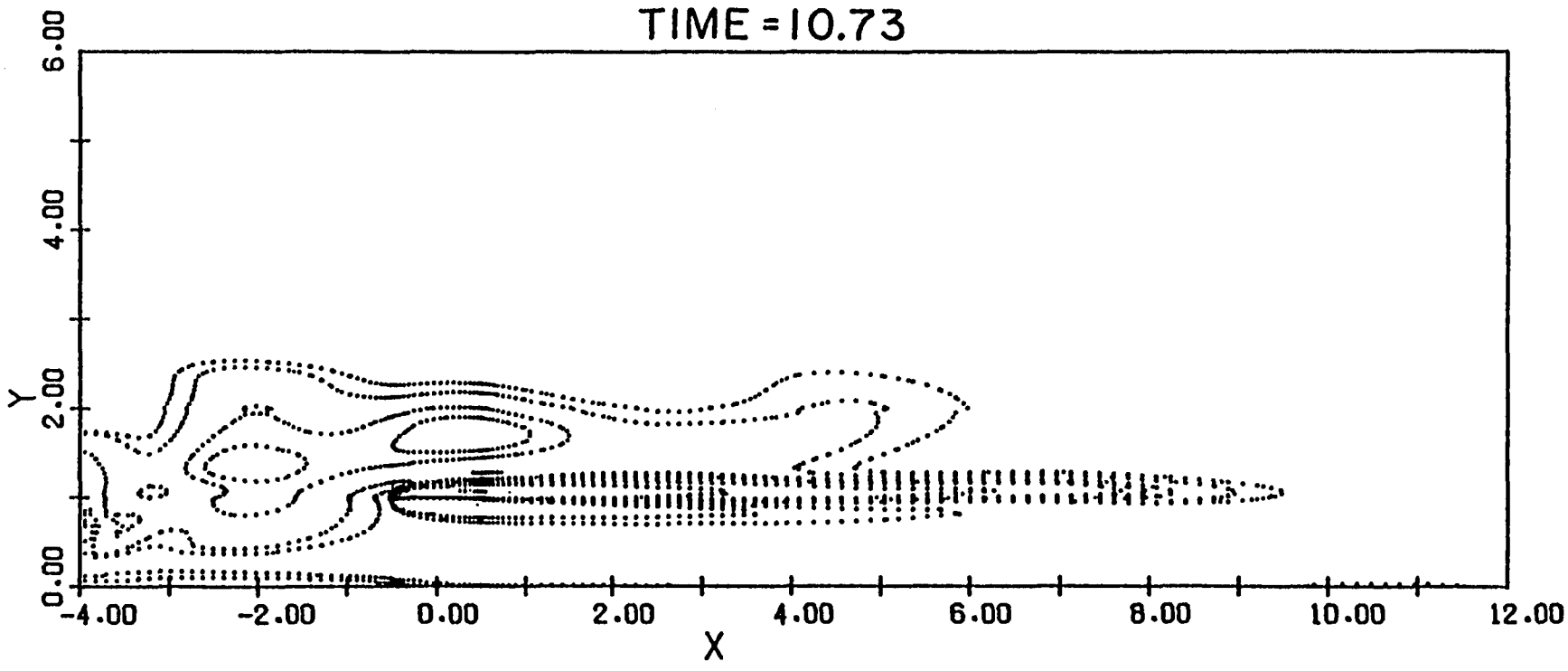

Fig. 13 Contours of Constant Perturbation Vorticity.
t = 10.73

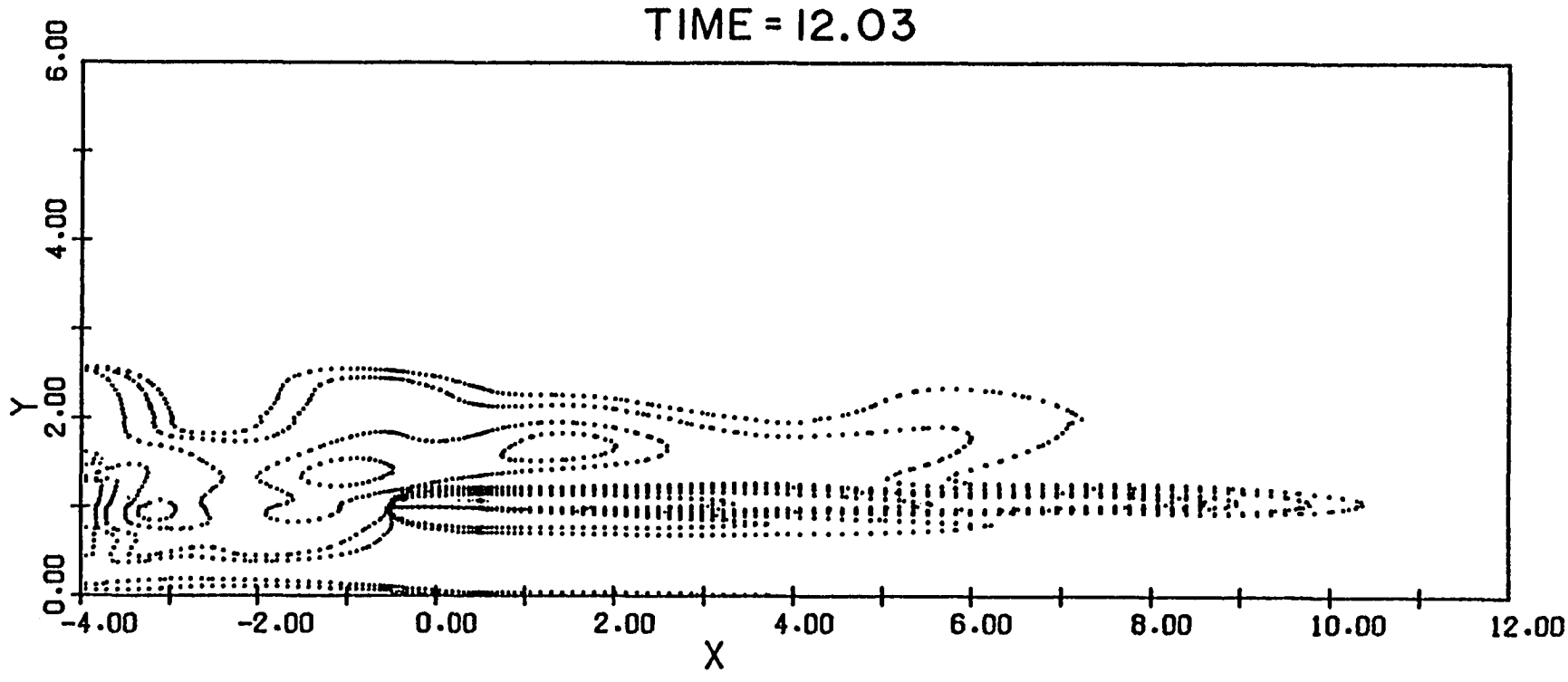

Fig. 14 Contours of Constant Perturbation Vorticity.
t = 12.03

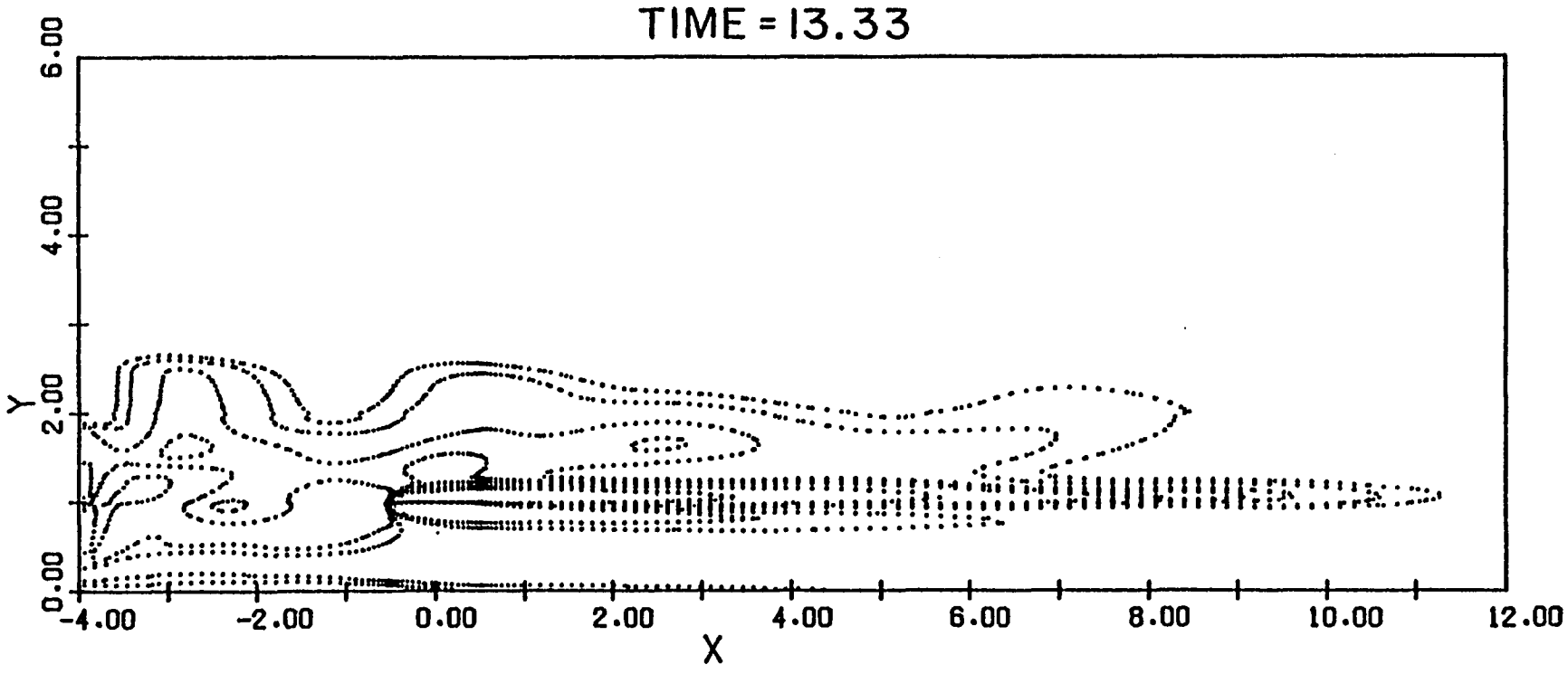

Fig. 15 Contours of Constant Perturbation Vorticity.
t = 13.33

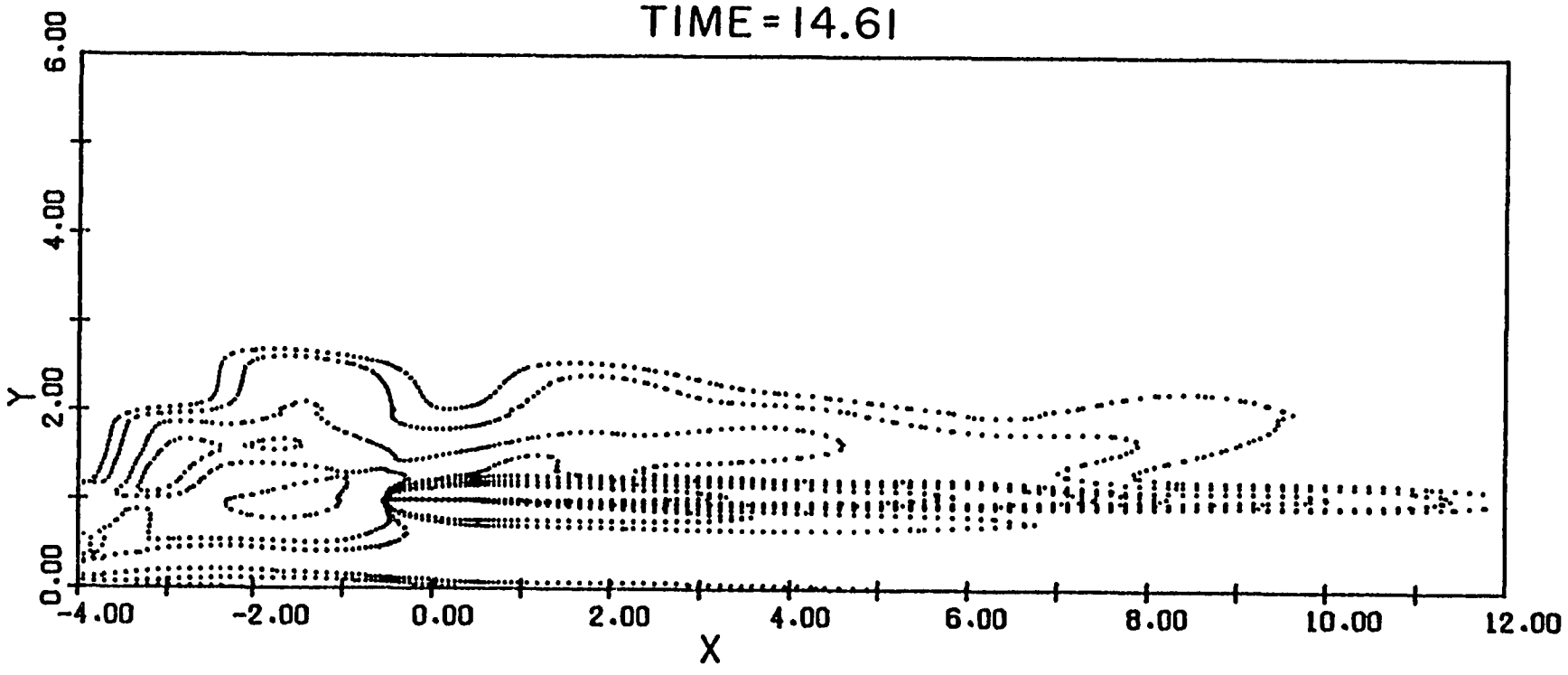

Fig. 16 Contours of Constant Perturbation Vorticity.
t = 14.61

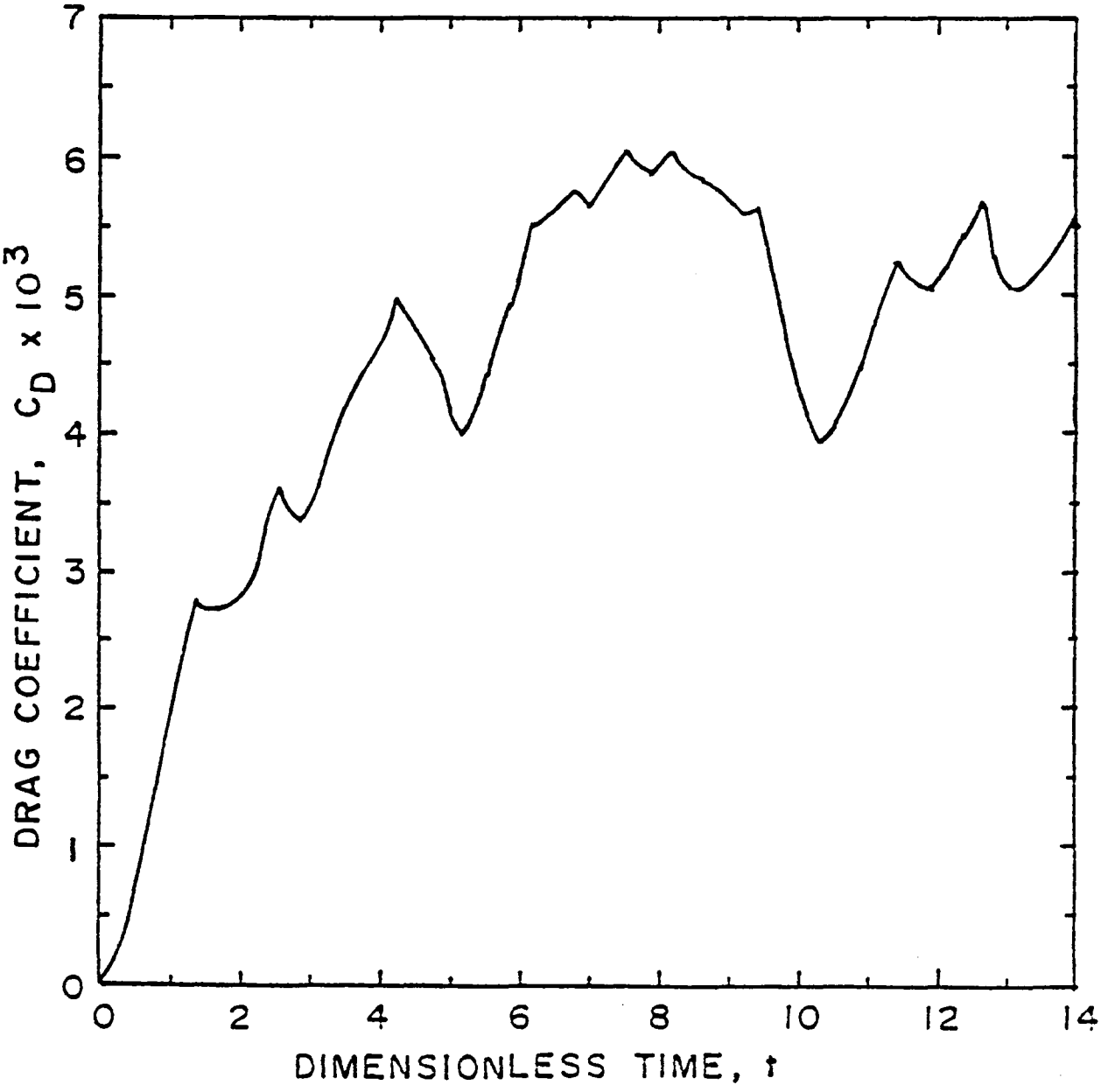

Fig. 17 Development of the Overall Drag Coefficient with Time

V. SUMMARY AND CONCLUDING REMARKS

Numerical solutions of the unsteady Navier-Stokes equations have been used to simulate large eddy breakup by a single flat plate imbedded in a wall boundary layer. The flow field has been treated as two-dimensional and incompressible.

The plate length has been taken to be one-half the boundary-layer thickness. The Reynolds number based on plate length was held fixed at 1000, giving a Reynolds number based on boundary-layer thickness of 2000.

The numerical simulation is essentially that of a laminar boundary layer undergoing transition to a turbulent boundary layer. Vorticity perturbations in the form of coherent eddies are swept into the computational domain. All of the eddies interact with one another and the background flow in a fully nonlinear fashion.

The eddy structures are altered by the plate imbedded in the boundary layer. The strong vorticity layers produced by the plate merge with the vorticity of the eddies, and the resultant wake persists for a long distance behind the plate. The coherent structures so evident ahead of the plate are nonexistent behind the plate. The straight appearance of the wake region reveals that there are no strong transverse velocities behind the plate. This is not the case ahead of the plate. Therefore, the plate effectively straightens the slow behind it, and high speed fluid above the plate does not penetrate the region close to the wall.

It is concluded that the plate does suppress the lateral mixing of the fluid in the boundary layer. This is consistent with the explanation given by Corke, Nagib, and Guezennec [1] for one of the mechanisms contributing to the drag reduction revealed by their experimental measurements. Although their measurements were made in a more highly developed turbulent flow than that simulated here, the fundamental conclusion is the same.

The present numerical simulation leaves unanswered the question of whether or not the plate actually reduces the total drag. To partially answer that question, one would need to perform a companion calculation with the same flow parameters, but with the plate absent. A comparison of the resulting drag curves would then show if the presence of the plate actually reduces drag.

Whereas the above-mentioned comparison would be of interest, it is beyond the scope of the current study. Also, the outcome would not be totally conclusive since many features of a turbulent flow are absent in the current simulation. The most important of these is the three-dimensional character of the flow. The introduction of a third dimension would allow the vorticity to change due to the stretching of vortex lines. That is, vorticity could increase locally. In the current calculations, vorticity only decreases due to the mechanism of diffusion. Local regions of enhanced vorticity cannot occur, and thus one mechanism for lateral mixing is completely absent.

ACKNOWLEDGEMENTS

The authors express their appreciation to Lona Howser and Jay Lambiotte of the STAR Computing Office of the Langley Research Center. They provided helpful consultations regarding the STAR operating system. Barbara Pitts assisted with the computer accounts and the exchanging of data files between NASA Langley and the University of Arizona. Bill Underhill of the University of Arizona wrote the computer code for the marker-and-cell calculations. Mrs. Margaret Wheeler of the Engineering Experiment Station oversaw the final preparation of this report.

APPENDIX A

SOLUTION ALGORITHM FOR THE STREAM FUNCTION

The algorithm is based on the Stabilized Error Vector Propagation method, as described briefly in Section III and Ref. [4]. The method is based on the observation that if the stream function is known on two adjacent rows, then it can be advanced to the next row. In this way, the solution can eventually be advanced to all the rows in the computational domain.

The governing equations for ψ are given by Eqns. (34), (44), (45), (46), and (47). We assume that

$$\psi_{i,j} = \hat{\psi}_{i,j} + \varepsilon_{i,j} \tag{A-1}$$

where $\hat{\psi}_{i,j}$ is the exact value, and $\varepsilon_{i,j}$ is an error term. Eqn. (A-1) is substituted into (37), (47), (48), and (49). The result is a set of algebraic equations for $\varepsilon_{i,j}$ For purposes of illustration, we assume a uniform grid with $\Delta x_i = \Delta y_j$. Then one has

$$\varepsilon_{i,j-1} = 4\varepsilon_{i,j} - \varepsilon_{i+1,j} - \varepsilon_{i-1,j} - \varepsilon_{i,j+1} \tag{A-2}$$

for $i \neq 1$, 141 and $j \neq 80$. For the nodes adjacent to boundaries, we have to make the following replacements,

$$\varepsilon_{i-1,j} = \frac{4\varepsilon_{i,j} - \varepsilon_{i+1,j}}{3} \tag{A-3}$$

$$\varepsilon_{i+1,j} = \frac{4\varepsilon_{i,j} - \varepsilon_{i-1,j}}{3} \tag{A-4}$$

$$\varepsilon_{i,j+1} = \varepsilon_{i,j} \tag{A-5}$$

Notice that the exact boundary conditions are enforced on the sides and top of the grid.

The main task is to trace the propagation of errors introduced at the top of the grid to the bottom of the grid, where a final boundary condition can be enforced. For example, consider the calculation illustrated in Table 1.

Table 1. Illustration of Error Propagation.

j \ i	1	2	3	4	5	6	7
80	0	0	1	0	0	0	0
79	0	-1	3	-1	0	0	0
78	2/3	-7	13	-7	1	0	0
77	52/9	-122/3	63	-41	11	-1	0
76	1130/27	-2020/9	962/3	-231	85	-15	1

A unit error introduced at i = 3, j = 80 propagates through the grid as shown. At j = 76, the error is already quite large.

Note that the error at any j is directly proportional to the error introduced at i = 3, j = 80. Let us first focus our attention on the error coefficient at i = 1, j = 76. In this case let us call it $a_{13} = 1130/27$. The first subscript denotes the column in which the error coefficient occurs, and the second denotes the column in which the unit error is introduced. If an error e_3 is introduced at i = 3 and j = 80, then the error at i = 1, j = 76 is $a_{13}\, e_3$.

Now observe that if the unit error had been introduced at i = 2, rather than i = 3, a different number would have occurred in the first column (i = 1) at j = 76. Call this the error coefficient, a_{12}. Likewise, we could generate different coefficients a_{1i} in the first column at j =76 for each unit error introduced at column i. The total error at node i = 1, j = 76 is thus

$$E_{1,76} = a_{11}e_1 + a_{12}e_2 + a_{13}e_3 + \cdots \qquad \text{(A-6)}$$

where only a_{13} has actually been computed in this example.

To obtain the error at j = 76 and i = 2, we need to generate coefficients a_{21}, a_{22}, a_{23}, etc. In this example, we have obtained only $a_{23} = -2020/9$, but one would have in analogy to (A-6)

$$E_{2,76} = a_{21}\ e_1 + a_{22}\ e_2 + a_{23}\ e_3 + \cdots \qquad \text{(A-7)}$$

and in general, one can write

$$E_{n,76} = a_{n1}\ e_1 + a_{n2}\ e_2 + a_{n3}\ e_3 + \cdots \qquad \text{(A-8)}$$

Thus we see that the a_{ni}'s form the error coefficients of an error propagation matrix. The complete error vector at Row 76 is just

$$[E_{76}] = [A]\,[e] \tag{A-9}$$

If we had wanted the error at Row 77, then we would have obtained a different error propagation matrix, [A].

The point to (A-9) is that we can relate the error introduced at one row to the error at any other row. For example, we guess the value of the stream function along the top row j = 80. For this study, it is assigned the arbitrary value of zero. The stream function is calculated by means of Eqns. (37), (47), (48), (49) until we reach the row along the wall, for which $\psi_{i,w}$ is given by (50). Now this row of values should all be zero, according to the boundary condition required at the wall. However, it won't be zero because an incorrect guess was made for $\psi_{i,80}$. In fact, the values of $\psi_{i,w}$ comprise the final error vector at the wall. Call this $[E_w]$. We then have by (A-9)

$$[E_w] = [A]\,[e] \tag{A-10}$$

$[E_w]$ and [e] are vectors with 140 elements. [A] is a square matrix. Since $[E_w]$ and [A] are known, we solved for [e] to get

$$[e] = [A]^{-1}\,[E_w] \tag{A-11}$$

Thus we have the error vector along the first row of nodes. This can be used to correct the values of $\psi_{i,80}$, which were initially guessed to be zero. Once the exact values of $\psi_{i,80}$ are known, the true solution for the stream function can be recalculated throughout the whole domain.

Thus there are two passes through the calculations, once the error coefficient matrix, [A], is generated. The first pass produces the error vector at the wall, and the second pass produces the stream function. Therefore it is a direct solution method. The advantages of this method are twofold. It is fast because it is noniterative. Also, the maximum-error can be found. This error is the deviation from zero of the final stream function value along the wall. Typically, the error is close to the computational precision of the computer.

There is a major disadvantage, however. The error matrix [A] can become so ill-conditioned that $[A]^{-1}$ is inaccurate, and thus the error calculated from (A-11) is inaccurate. This happens when there are many rows in the grid. To handle such cases, the grid has to be broken down into blocks. This allows the error to be stabilized.

The algorithm used for the Stabilized Error Vector Propagation (SEVP) method is illustrated here by the use of three blocks, as shown in Fig. A-1. It can be generalized to any number of blocks. Note that adjacent blocks overlap by two rows. The values for the stream function are guessed on dashed lines. Boundary values for the stream function are given on solid lines. Suppose each block is 8 rows long. We start at the top of the first block.

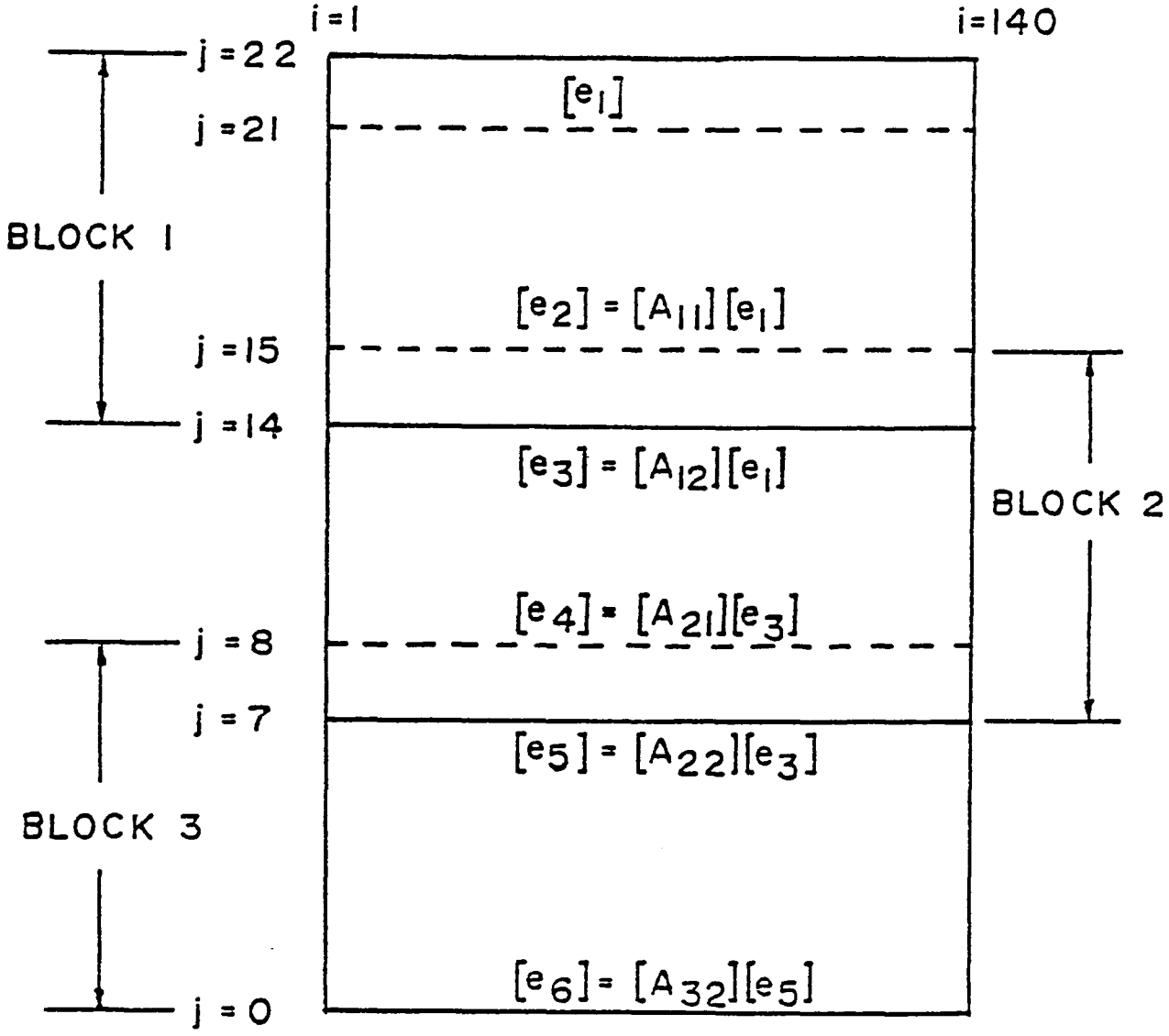

Fig. A-1 Illustration of the Use of Blocks in the Stabilized Error Vector Propagation Method

Error propagation matrices $[A_{11}]$, $[A_{12}]$, $[A_{21}]$, $[A_{22}]$, and $[A_{32}]$ must first be generated. This can be done once and the results stored for later use. We first specify 140 unit vectors on j = 21, j = 14, and j = 7. Recall that this is done by making an entry of unity at one of the columns i; all other entries being zero. We then calculate the errors by Eqns. (A-2) through (A-5) at each of the j rows. This requires "boundary values" for the errors to be specified at j = 15 and j = 8. Eqn. (A-5) is enforced for j = 21 only, since this is a true boundary for the grid.

Calculations begin in the first block, and $[A_{11}]$ and $[A_{12}]$ are obtained. Clearly, $[e_2] = [A_{11}]\,[e_1]$ and $[e_3] = [A_{12}][e_1]$. Then $[e_1] = [A_{12}]^{-1}\,[e_3]$, whereupon

$$[e_2] = [A_{11}]\,[A_{12}]^{-1}\,[e_3] = [B_1]\,[e_3] \tag{A-12}$$

We now introduce unit vectors along j = 14 and enforce values of $[e_2]$ obtained from (A-12) along j = 15. We thus march to Rows j = 8 and j = 7 and obtain $[A_{21}]$ and $[A_{22}]$. Once again

$$[e_4] = [A_{21}]\,[e_3] = [A_{21}]\,[A_{22}]^{-1}\,[e_5] = [B_2]\,[e_5] \tag{A-13}$$

Unit vectors are introduced along j = 7, and corresponding boundary values $[e_4]$ are calculated from (A-13) and enforced along j = 8. The solution for the error vectors is again extended into the third block to j = 0. This gives $[A_{32}]$.

Error propagation matrices $[A_{11}]$, $[A_{12}]$, $[A_{21}]$, $[A_{22}]$ and $[A_{32}]$, and corresponding matrices $[B_1]$ and $[B_2]$ are now all known and stored once

and for all. It remains to find an approximate solution for the stream function. This requires two forward sweeps through each of the blocks. A final backward (correction) sweep through the entire grid produces the exact solution.

We start by guessing the stream function to be zero along Row j = 21 and use the boundary condition at j = 22. We march the solution forward to j = 15 and 14. Along j = 14, we must enforce a pseudo-boundary condition, which we choose to be $\psi = 0$. The departure from zero of the calculated value of ψ on j = 14 gives $[e_3]$.

Next, we obtain $[e_1] = [A_{12}]^{-1} [e_3]$. With this we correct the solution for ψ along j = 21, and we generate stream functions over the first block and into the second block until we reach j = 7. We again enforce the pseudo-boundary condition of $\psi = 0$ here, and obtain the error vector $[e_5]$. From this we find $[e_3] = [A_{22}]^{-1} [e_5]$ and $[e_2] = [B_1] [e_3]$. With these boundary values, we now correct the stream function along j = 15 and 14 in the second block and proceed to march ψ through the second and third blocks. The process is repeated until we have swept all the blocks.

For the last block, we use the exact boundary condition of $\psi = 0$ on j = 0 to find $[e_6]$. Then $[e_5] = [A_{32}]^{-1} [e_6]$ and $[e_4] = [B_2] [e_5]$. The solution for ψ is corrected on j = 7 and 8 and marched through the last block to j = 0.

At this stage we have the <u>exact</u> solution for ψ over the last block. It remains to extend the solution, along with new error vectors, over the second and first blocks. For this we obtain a new error vector $[e_5]$ by subtracting the exact solution for ψ at j = 7 from the approximate

solution generated at j = 7 during the forward sweep of Blocks 2 and 3. Note that this approximate solution along j = 7 was stored with forethought. We now recalculate $[e_3] = [A_{22}]^{-1} [e_5]$ and $[e_2] = [B_1] [e_3]$. Then, the approximate solutions at j = 14 and 15 (again stored with forethought) are corrected and the new exact solution for ψ is marched from j = 15 to j = 7. A new error vector $[e_3]$ is obtained by subtracting the exact solution on j = 14 from the approximate solution stored at j = 14 from the forward sweep through Blocks 1 and 2. Finally, $[e_1] = [A_{12}]^{-1} [e_3]$, and the approximate solution on j = 21 is corrected. The boundary condition along the top of the grid is applied to find ψ along j = 22. The final sweep from j = 22 to j = 14 completes the generation of the exact solution.

The solution generated by this direct method is discontinuous at block boundaries (j = 14 and 7), and it may not satisfy the exact boundary condition of $\psi = 0$ along j = 0. The amount of discontinuity and the departure from $\psi = 0$ on j = 0 gives a measure of the <u>maximum</u> error. Typically, the maximum error can be controlled to the round-off error of the calculations. Iterations can be used to reduce errors further, but they were not used in this present study.

In this work, fourteen blocks were used. The first ten blocks had eight rows each, and the remainder had seven rows. The maximum error on j = 0 was 1.1×10^{-11} at i = 36. Most of the errors were on the order of 10^{-15} along j = 0. Errors at the block boundaries were not checked.

APPENDIX B

INTERPOLATION METHOD FOR STREAM FUNCTION

The interpolation procedure involves a nine-point formula in x and y. To proceed, we assume a biquadratic formula of the following type:

$$\psi = a + bx + cy + dxy + ex^2 + fy^2 + gx^2y + hxy^2 + ix^2y2 \qquad \text{(B-1)}$$

Here, x and y denote <u>local</u> coordinates, with origin at Point 1, as shown in Fig. B-1.

In principle, one can find the nine unknown constants a through i from known values of ψ at nine points in the field. However, the solution of the nine simultaneous equations would be tedious, and we do want a closed form solution. Instead, we utilize a procedure used in finite-element analysis.

We note that the x- and y-spacing is variable and construct polynomials in x as follows:

$$N_1(x) = \frac{(x-h_1)(x-h_1-h_2)}{h_1(h_1+h_2)} \qquad \text{(B-2)}$$

$$N_2(x) = \frac{-x(x-h_1-h_2)}{h_1h_2} \qquad \text{(B-3)}$$

$$N_3(x) = \frac{x(x-h_1)}{(h_1+h_2)h_2} \qquad \text{(B-4)}$$

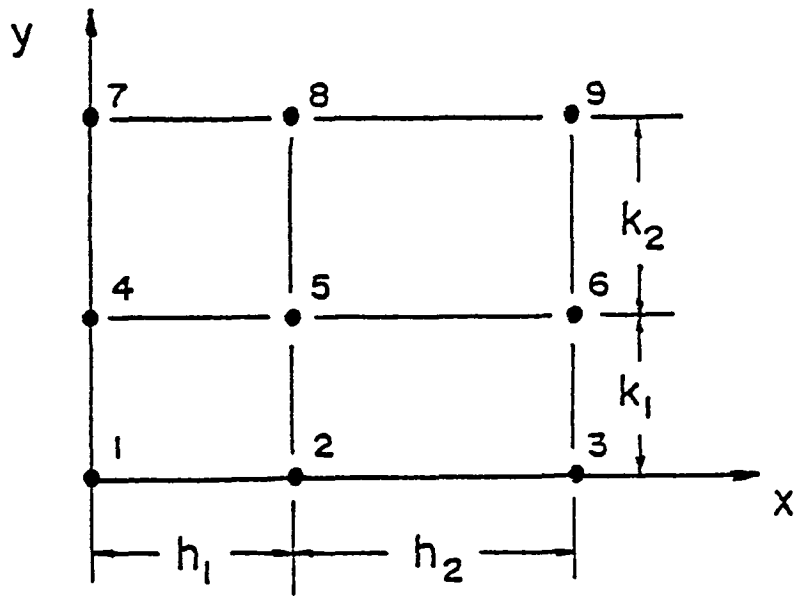

Fig. B-1 Illustration of Node Arrangement Used in the Nine-Point Interpolation Method for the Stream Function

These expressions have the following properties:

$$N_1(0) = 1 \quad , \quad N_1(h_1) = N_1(h_1+h_2) = 0$$

$$N_2(h_1) = 1 \quad , \quad N_2(0) = N_2(h_1+h_2) = 0$$

$$N_3(h_1+h_2) = 1 \quad , \quad N_3(0) = N_3(h_1+h_2) = 0$$

Next, we form identical polynomials in y, but with h_1 replaced by k_1, etc. The final expression for ψ becomes

$$\begin{aligned}\psi = & [\omega_1 N_1(x) + \omega_2 N_2(x) + \omega_3 N_3(x)] N_1(y) \\ & + [\omega_4 N_1(x) + \omega_5 N_2(x) + \omega_6 N_3(x)] N_2(y) \\ & + [\omega_7 N_1(x) + \omega_8 N_2(x) + \omega_9 N_3(x)] N_3(y)\end{aligned} \tag{B-5}$$

Next, Eqn. (B-5) is expanded, and terms are collected. After extensive algebra, one can obtain the coefficients a through i by inspection. The results are:

$$a = \omega_1 \tag{B-6}$$

$$b = \frac{-(2h_1+h_2)}{h_1(h_1+h_2)}\omega_1 + \frac{h_1+h_2}{h_1h_2}\omega_2 - \frac{h_1}{h_2(h_1+h_2)}\omega_3 \tag{B-7}$$

$$c = \frac{-(2k_1+k_2)}{k_1(k_1+k_2)}\omega_1 + \frac{k_1+k_2}{k_1k_2}\omega_4 - \frac{k_1}{k_2(k_1+k_2)}\omega_7 \tag{B-8}$$

$$d = \frac{(2h_1+h_2)\ (2k_1+k_2)}{h_1k_1(h_1+h_2)(k_1+k_2)}\omega_1 - \frac{(h_1+h_2)(2k_1+k_2)}{h_1h_2k_1\ (k_1+k_2)}\ \omega_2$$

$$+ \frac{h_1(2k_1+k_2)}{k_1h_2(h_1+h_2)(k_1+k_2)}\ \omega_3 - \frac{(2h_1+h_2)(k_1+k_2)}{h_1k_1k_2(h_1+h_2)}\ \omega_4$$

$$+ \frac{(h_1+h_2)(k_1+k_2)}{h_1h_2\ k_1k_2}\ \omega_5 - \frac{h_1(k_1+k_2)}{h_2k_1k_2(h_1+h2)}\ \omega_6$$

$$+ \frac{k_1(2h_1+h_2)}{h_1k_2(h_1+h_2)(k_1+k_2)}\omega_7 - \frac{(h_1+h_2)k_1}{h_1h_2(k_1+k_2)}\ \omega_8 + \frac{h_1k_1}{h_2k_2(h_1+h_2)(k_1+k_2)}\ \omega_9 \quad \text{(B-9)}$$

$$e = \frac{1}{h_1(h_1+h_2)}\ \omega_1 - \frac{1}{h_1h_2}\ \omega_2 + \frac{1}{h_2(h_1+h_2)}\ \omega_3 \quad \text{(B-10)}$$

$$f = \frac{1}{k_1(k_1+k_2)}\ \omega_1 - \frac{1}{k_1k_2}\ \omega_4 + \frac{1}{k_2(k_1+k_2)}\ \omega_7 \quad \text{(B-11)}$$

$$g = \frac{-(2k_1+k_2)}{h_1k_1(h_1+h_2)(k_1+k_2)}\ \omega_1 + \frac{2k_1+k_2}{h_1h_2k_1(k_1+k_2)}\ \omega_2 - \frac{2k_1+k_2}{k_1h_2(h_1+h_2)(k_1+k_2)}\ \omega_3$$

$$+ \frac{k_1+k_2}{h_1k_1k_2(h_1+\ h_2)}\ \omega_4 - \frac{k_1+k_2}{h_1h_2k_1k_2}\ \omega_5 + \frac{k_1+k_2}{h_2k_1k_2(h_1+h_2)}\ \omega_6$$

$$- \frac{k_1}{h_1k_2(h_1+h_2)(k_1+k_2)}\ \omega_7 + \frac{k_1}{h_1h_2k_2(k_1+k_2)}\ \omega_8 - \frac{k_1}{h_2k_2(h_1+h_2(k_1+k_2)}\ \omega_9 \quad \text{(B-12)}$$

$$h = \frac{-(2h_1+h_2)}{h_1k_1(h_1+h_2)(k_1+k_2)}\ \omega_1 + \frac{h_1+h_2}{h_1h_2k_1(k_1+k_2)}\ \omega_2 - \frac{h_1}{k_1h_2(h_1+h_2)(k_1+k_2)}\ \omega 3$$

$$+ \frac{2h_1+h_2}{h_1k_1k_2(h_1+h_2)}\ \omega_4 - \frac{h_1+h_2}{h_1h_2k_1k_2}\ \omega_5 + \frac{h_1}{h_2k_1k_2(h_1+h_2)}\omega_6$$

$$- \frac{2h_1+h_2}{h_1k_2(h_1+h_2)(k_1+k_2)}\omega_7 + \frac{h_1+h_2}{h_1h_2k_2(k_1+k_2)}\ \omega_8 - \frac{h_1}{h_2k_2(h_1+h_2)(k_1+k_2)}\ \omega_9 \quad \text{(B-13)}$$

$$i = \frac{\omega_1}{h_1 k_1 (h_1+h_2)(k_1+k_2)} - \frac{\omega_2}{h_1 h_2 k_1 (k_1+k_2)} + \frac{\omega_3}{k_1 h_2 (h_1+h_2)(k_1+k_2)}$$

$$- \frac{\omega_4}{h_1 k_1 k_2 (h_1+h_2)} + \frac{\omega_5}{h_1 h_2 k_1 k_2} - \frac{\omega_6}{h_2 k_1 k_2 (h_1+h_2)}$$

$$+ \frac{\omega_7}{h_1 k_2 (h_1+h_2)(k_1+k_2)} - \frac{\omega_8}{h_1 h_2 k_2 (k_1+k_2)} + \frac{\omega_9}{h_2 k_2 (h_1+h_2)(k_1+k_2)} \qquad \text{(B-14)}$$

The spacings h_1, h_2, etc. are obtained from the nodal arrangement shown in Fig.3; that is, $h_1 = .5\ (\Delta x_{i-1} + \Delta x_i)$ etc.

REFERENCES

1. Corke, T. C.; Nagib, H. M.; and Guezennec, Y. G.: A New View of Origin, Role, and Manipulation of Large Scales in Turbulent Boundary Layers. NASA CR-165861, February 1982.

2. Schmall, R. A.; and Kinney, R. B.: Numerical Study of Unsteady Viscous Flow Past a Lifting Plate. AIAA Journal, Vol. 12, November 1974, pp. 1566-1573.

3. Schlichting, H. A.: Boundary Layer Theory, 7th Edition, McGraw-Hill Book Company, New York, 1979.

4. Madala, R. V.; and McDonald, B. E.: "Solution of Elliptic Equations," Chapter 7, Finite-Difference Techniques for Vectorized Fluid Dynamics Calculations, David L. Book, Editor, Springer-Verlag, New York, 1981.

5. Madala, R. V.: An Efficient Direct Solver for Separable and Nonseparable Elliptic Equations. Monthly Weather Review, Vol. 106, 1978, pp. 1735.

6. Roache, P. J.: Computational Fluid Dynamics, Hermosa Publishers, Albuquerque, New Mexico, 1972.

7. Taslim, M. E.; Kinney, R. B.; and Paolino, M. A.: Analysis of Two-Dimensional Viscous Flow over Cylinders in Unsteady Motion. AIAA Journal, Vol. 22, May 1984, pp. 586-594.

8. Welch, J. E.; Harlow, F. H.; Shannon, J. P.; and Daly, B. J.: The MAC Method, A Computing Technique for Solving Viscous, Incompressible, Transient Fluid-Flow Problems Involving Free Surfaces. Los Alamos Scientific Lab. Report LA-3425, New Mexico, March 1966.

1. Report No.	2. Government Accession No.	3. Recipient's Catalog No.
NASA CR-3884		

4. Title and Subtitle	5. Report Date
Numerical Study of Large-Eddy Breakup and Its Effect on the Drag Characteristics of Boundary Layers	March 1985
	6. Performing Organization Code

7. Author(s)	8. Performing Organization Report No.
Robert B. Kinney, Mohammad E. Taslim, and Shi Chang Hung	
	10. Work Unit No.

9. Performing Organization Name and Address	11. Contract or Grant No.
The University of Arizona Department of Aerospace and Mechanical Engineering Tucson, AZ 85721	NAG1-141
	13. Type of Report and Period Covered
12. Sponsoring Agency Name and Address	Contractor Report
National Aeronautics and Space Administration Washington, DC 20546	14. Sponsoring Agency Code
	505-31-13-05

15. Supplementary Notes

Langley Research Center Technical Monitor: Jerry N. Hefner
FINAL REPORT

16. Abstract

The break-up of a field of eddies by a flat-plate obstacle embedded in a incompressible and unsteady boundary layer is studied using numerical solutions to the two-dimensional Navier-Stokes equations. Results show that the eddies are broken up by the plate. The strong wake generated by the plate prevents the eddy vorticity from penetrating the region between the plate and wall as the eddies are swept downstream. Transverse velocities evident ahead of the plate are absent behind the plate. Thus, it appears that high speed outer fluid is prevented by the plate from being entrained into the fluid layer near the wall. This has been proposed to be one of the mechanisms by which break-up devices can reduce drag locally. The numerical predictions support this proposal.

17. Key Words (Suggested by Author(s))	18. Distribution Statement
Viscous Drag Reduction Turbulence Control Numerical Navier-Stokes Solutions	Unclassified - Unlimited Subject Category 34

19. Security Classif. (of this report)	20. Security Classif. (of this page)	21. No. of Pages	22. Price
Unclassified	Unclassified	90	A05

For sale by the National Technical Information Service, Springfield, Virginia 22161

NASA-Langley, 1985